Divergent sensory processing converges in frontal cortex for a planned motor response

Vahid Esmaeili[1,3,*], Keita Tamura[1,3,*], Samuel P. Muscinelli[1,2], Alireza Modirshanechi[1], Marta Boscaglia[1], Ashley B. Lee[1], Anastasiia Oryshchuk[1], Georgios Foustoukos[1], Yanqi Liu[1], Sylvain Crochet[1], Wulfram Gerstner[1] and Carl C.H. Petersen[1,*,‡]

[1] Brain Mind Institute, Faculty of Life Sciences, École Polytechnique Fédérale de Lausanne (EPFL), Lausanne, Switzerland

[2] Current address: Center for Theoretical Neuroscience, Zuckerman Institute, Columbia University, 10027 New York, USA

[3] Contributed equally to this study.

* Corresponding authors:
vahid.esmaeili@epfl.ch
keita.tamura@epfl.ch
carl.petersen@epfl.ch

‡ Lead contact:
Carl Petersen,
Laboratory of Sensory Processing,
Brain Mind Institute, Faculty of Life Sciences,
SV-BMI-LSENS Station 19,
Ecole Polytechnique Fédérale de Lausanne (EPFL),
CH-1015 Lausanne, Switzerland.
Tel: +41 21 693 1721
E-mail: carl.petersen@epfl.ch

SUMMARY

Purposeful behavior requires planning of actions based on external information. However, neuronal mechanisms converting sensory input into a motor plan remain elusive. Here, we combined wide-field calcium imaging, multi-area single-neuron recordings and focal optogenetic inactivation to reveal the precise sequence of cortical activity transforming sensory information into motor planning in mice trained to respond to a brief whisker stimulus by licking after a delay. We found that upon learning, the sensory information, initially highly-localized, rapidly spreads to diverse motor and higher-order areas, together with transient deactivation of orofacial regions, converging during the delay period to a focalized region of the frontal cortex. The secondary whisker motor cortex (wM2) appears as a key relay of this sensorimotor transformation, showing the earliest learning-enhanced response to the whisker stimulus. Our results suggest a specific cortical circuit with wM2 acquiring a pivotal role in transforming whisker information into preparatory activity for goal-directed motor planning.

Keywords

Reward-based learning, sensorimotor transformation, whisker somatosensation, multisensory processing, motor planning and execution, working memory, cortical circuits, electrophysiology, calcium imaging, optogenetics

Highlights

- **Cortex-wide, task-epoch specific causal neuronal dynamics of sensorimotor learning**
- **Sensory information converges to a focal frontal region critical for delay-response**
- **Orofacial cortex acquired an inhibitory response with delayed lick learning**
- **Secondary whisker motor cortex is a key node converting whisker input to lick plan**

INTRODUCTION

Incoming sensory information is processed in a learning- and context-dependent manner to direct goal-directed behavior, but the underlying neural circuit mechanisms are poorly understood. To dissect this process, it would be crucial to follow the causal chain of neuronal activity across brain areas as sensory information is transformed into goal-directed motor output (de Lafuente and Romo, 2006) and to examine how the underlying sensory and motor circuits become connected through learning. Investigations of head-restrained behaving mice offer increasingly-detailed insights into mammalian brain function through precise stimulus control and monitoring of behavior (Carandini and Churchland, 2013), along with increasingly-sophisticated methods for measuring and manipulating neuronal activity (Luo et al., 2018; Pinto et al., 2019; Steinmetz et al., 2019).

Rodents gather extensive information about their immediate environment through their array of whiskers surrounding the snout (Bosman et al., 2011; Diamond et al., 2008; Feldmeyer et al., 2013; Petersen, 2019). Tactile information from whiskers is relayed to whisker somatosensory cortex (wS1) where each whisker is represented by an anatomically-defined unit, termed a barrel, forming a well-defined starting point for cortical processing of whisker-related sensory information. Although rodents can perform simple whisker-dependent tasks after permanent lesioning of wS1 (Hong et al., 2018; Hutson and Masterton, 1986), transient inactivation of wS1 impairs performance in tasks where they are trained to detect a brief whisker deflection (Hong et al., 2018; Miyashita and Feldman, 2013; Sachidhanandam et al., 2013; Yang et al., 2016). Whisker-detection task learning appears to be accompanied by a strengthening of interactions between wS1 and secondary whisker somatosensory cortex (wS2) (Kwon et al., 2016; Yamashita and Petersen, 2016), as well as the recruitment of multiple other brain regions (Kyriakatos et al., 2017; Le Merre et al., 2018; Sippy et al., 2015).

The simplest whisker-detection tasks allow mice to lick immediately after the whisker stimulus, giving rise to neuronal activity related to sensory, choice and motor components of behavior, which are difficult to disentangle (Musall et al., 2019). Imposing a delay between the presentation of the sensory stimulus and the motor response can help to better distinguish such mixed computations. Previous studies have reported prominent delay period activity in broad regions of frontal cortex (Chabrol et al., 2019; Chen et al., 2017; Erlich et al., 2011; Esmaeili and Diamond, 2019; Fassihi et al., 2017; Funahashi et al., 1989; Fuster and Alexander, 1971; Guo et al., 2014; Li et al., 2015; Makino et al., 2017; Tanji and Evarts, 1976). However, the various roles of distinct subregions of frontal cortex has not been studied in detail for any specific sensorimotor delay task across learning. Furthermore, the precise circuit mechanisms that give rise to such preparatory neuronal activity during the delay period in response to a sensory stimulus across learning remains to be investigated. Moreover, recent studies suggest that uninstructed movements may contribute prominently to widespread neuronal activity (Musall et al., 2019; Stringer et al., 2019), and may be an important confound during many delayed-response tasks where preparatory movements could help animals to bridge the delay period. Thus, neuronal delay activity in some regions might reflect preparatory movement itself rather than the motor plan.

Here, we introduce a delayed whisker-detection learning paradigm and through a unified analysis by high-speed calcium imaging, large-scale neurophysiological recordings, temporally specific optogenetic inactivation and rigorous behavioral and analytical methods we detail the spatiotemporal map of causal cortical processing accompanying learning. We find causal contributions for initially localized sensory processing in wS1/wS2 rapidly spreading to multiple downstream cortical areas and converging in secondary tongue/jaw anterolateral motor cortex (tjM2/ALM), with the earliest learning-enhanced choice-related neuronal activity being found in the secondary whisker motor cortex (wM2).

RESULTS

Behavioral changes accompanying delayed-response task learning

To study essential neuronal mechanisms for reward-based sensorimotor transformation, we designed a well-controlled Go/No-Go learning paradigm where head-restrained mice learned to lick in response to a whisker stimulus after a one second delay period (Figure 1A-C). To precisely track the sequence of cortical responses, we used a single, short (10 ms) deflection of C2 whisker. To uncover changes specific to the coupling of the whisker stimulus with the licking response, a two-phase learning paradigm was implemented: the "Pretraining" included only one trial type; trials were separated 6-8 seconds and started after mice withheld licking for a variable "Quiet" window of 2-3 seconds. A visual and an auditory cue, separated by 2 seconds, signaled the start and end of each trial. Only licking after the auditory cue was rewarded, while licking before the auditory cue ("early lick") aborted the trial with a time-out punishment. The "Pretraining" stablished a basis for the task, where mice learned the general task structure while no whisker stimulus was delivered yet. In the second phase, "Whisker training", in half of trials (referred to as "Go" trials), the whisker stimulus was introduced one second after the visual onset and omitted in the other half ("No-Go" trials); only licking after the auditory cue in Go trials was rewarded. Early licks in all trials and licking in No-Go trials were punished with a time-out, resulting in longer inter-trial-intervals (Figure 1B). Thus, mice were required to withhold licking to initiate trials, detect the whisker stimulus in Go trials, remember it over a one second delay period, and lick after the auditory go cue was presented. This design allowed us to compare behavior and neuronal activity of mice before ("Novice") and after ("Expert") the whisker training phase. Both Novice and Expert mice were recorded in the final task conditions (Figure 1C, for details see STAR Methods).

We quantitatively monitored the behavior of mice using a piezoelectric lick sensor and high-speed video filming (Figure 1A). The whisker training induced both instructed and uninstructed behavioral changes (Figures 1D-F and S1). Novice mice licked equally in Go and No-Go trials, but Expert mice had learned to lick preferentially in Go trials (Figures 1D left and S1A; Novice, p=0.85, n=15 mice; Expert, p<0.001, n=25 mice; Wilcoxon signed-rank test). Expert mice made more early licks (in Go-trials) compared to Novice mice (Figures 1D right and S1B; p=0.02, Wilcoxon rank-sum test) and had shorter reaction times in completed Go trials (Hit) compared to No-Go trials (False-alarm) (Figure S1B; Novice, p=0.14, Expert, p<0.01; Wilcoxon signed-rank test). This indicates that Expert mice used whisker information to make correct decisions, and predicted the timing of the auditory cue while avoiding early licks in the majority of trials. After whisker training, mice also adopted new movement strategies (Figures 1E-F, S1C-D). In Hit trials, mice decreased whisker movement before whisker stimulus, possibly to improve the detection of passively-applied whisker stimuli in the "receptive mode" (Diamond and Arabzadeh, 2013; Kyriakatos et al., 2017). The whisker, tongue and jaw movements after whisker stimulus increased in Hit trials, reflecting preparation for licking. These anticipatory movements were absent in Miss and Correct-rejection trials (Figure S1C).

Emergence of cortical activation and deactivation patterns through whisker training

The delay-task enables the investigation of different aspects of neuronal computations underlying reward-based behavior including: sensory processing, motor planning and motor execution in well-isolated time windows. As a first step, we mapped the spatiotemporal dynamics of cortical activity by wide-field calcium imaging at a high temporal resolution (100 frames per second, Figures 2 and S2). In transgenic mice expressing a fluorescent calcium indicator in pyramidal neurons (RCaMP mice) (Bethge et al., 2017), functional images of the left dorsal cortex were obtained through an intact skull preparation, and registered to the Allen Mouse Brain Common Coordinate Framework (Figure 2A-B) (Lein et al., 2007; Wang et al., 2020).

To examine the changes in cortical processing upon learning, we compared in the same mice the activity in correct trials before (Novice, 62 sessions) and after (Expert, 82 sessions) whisker training (Figures 2C-E for Hit trials and S2A-B for Correct-rejection trials, Videos S1-2). The visual cue evoked responses in the primary visual (Vis) and surrounding areas (Andermann et al., 2011; Marshel et al., 2011; Wang and Burkhalter, 2007), which decreased significantly after whisker training (Figures 2C and S2A; subtraction between Novice and Expert mice images, threshold $p<0.05$, Wilcoxon rank-sum test, with false discovery rate (FDR) correction; for details, see STAR Methods). Stimulation of the C2 whisker evoked two focal responses, one in the primary and the other in the secondary whisker somatosensory areas (wS1, wS2), both in Novice and Expert mice (Figure 2C and D top). After this initial sensory response, only in Expert mice, activity decreased transiently in broad orofacial areas including the primary tongue/jaw sensory and motor areas (tjS1, tjM1) (Figures 2C and 2D) followed by a wide-spread gradual increase toward the auditory cue initiating in the primary and secondary motor areas for whisker (wM1, wM2) and tongue/jaw (tjM1, tjM2/ALM), as well as posterior parietal cortex (PPC) and limb/trunk areas (Figure 2C and E). Those positive and negative responses during the delay period were selective to Hit trials of Expert mice (Figures 2C-E, S2C-F, and Videos S3-4; threshold $p<0.05$, Wilcoxon rank-sum test, FDR-corrected) similarly to the preparatory orofacial movements (Figures 1E-F and S1C-D). This selectivity suggests that the bipolar cortical responses might be involved in the correct whisker detection and the delayed-licking acquired through whisker training.

To control for hemodynamic effects of the wide-field fluorescence signal, we also imaged transgenic mice expressing an activity-independent red fluorescent protein, tdTomato (Figure S3A-B; 57 sessions from 7 Expert mice). The tdTomato control mice showed significantly smaller signals than the RCaMP mice did (subtraction between RCaMP and tdTomato mice images, threshold $p<0.05$, Wilcoxon rank-sum test, FDR-corrected). In visual cortex of both RCaMP and tdTomato mice, negative intrinsic signals were evoked around 1 s after the visual stimulus. However, the whisker stimulation evoked the rapid positive sensory response only in RCaMP mice, and no clear response was evoked in tdTomato mice likely because of the weak stimulation amplitude. On the other hand, some positive intrinsic optical signals were evoked in midline and frontal regions of tdTomato mice, but the amplitude of these signals was significantly smaller than for RCaMP mice (threshold $p<0.05$, Wilcoxon rank-sum test, FDR-corrected). These results suggest that the spatiotemporal patterns of fluorescence signals in RCaMP mice largely reflected the calcium activity of the cortex.

Distinct modification of early and late whisker processing in single neurons

To further investigate learning-related cortical dynamics at the level of spiking activity of single units and with higher temporal resolution we carried out large-scale silicon probe recordings (Buzsáki, 2004). Our recordings targeted 12 brain regions with guidance from wide-field calcium imaging (Figures 2 and S2), optical intrinsic imaging and previous literature (Esmaeili and Diamond, 2019; Guo et al., 2014; Harvey et al., 2012; Kyriakatos et al., 2017; Le Merre et al., 2018; Mayrhofer et al., 2019; Sippy et al., 2015; Sreenivasan et al., 2016): visual (Vis), whisker somatosensory (wS1 and wS2) and auditory (Aud) cortices; motor areas related to whisker (wM1 and wM2) and tongue/jaw (tjM1 and tjM2/ALM); the dorsolateral region of striatum (DLS) innervated by wS1; higher-order areas of posterior parietal cortex (PPC), medial prefrontal cortex (mPFC) and a dorsal part of hippocampal area CA1 (dCA1) (Figures 3A and S4A). In any given session we recorded from two areas simultaneously, and the precise anatomical location was determined by reconstructing three-dimensional coordinates of the silicon probe tracks through histological analysis, two-photon tomography, and registration to the Allen atlas (Figures 3A and S4A; for details, see STAR Methods) (Lein et al., 2007; Wang et al., 2020). In total, we recorded 4,415 regular spiking units (RSUs) in 22 Expert mice, and 1,604 RSUs in 8 Novice mice.

Single neurons in different areas fired spikes in specific moments of the task such as whisker sensory processing, lick preparation and lick execution (Figure 3B). To reveal neuronal firing changes through whisker training, we calculated time-dependent mean firing rate for all recording probes (Figure 3C and Videos S5-6) and for the 12 anatomically defined areas (Figure 3D). The visual cue evoked a long-lasting response in Vis and PPC of Novice and Expert mice. The whisker stimulus evoked an early wide-spread excitation across whisker sensorimotor areas (wS1, wS2, wM1, wM2), as well as PPC, DLS and tjM2/ALM. Following the auditory cue, excitation rapidly covered all recorded regions.

Major changes by whisker training appeared in the delay period between the whisker and auditory stimuli. The initial excitation was significantly enhanced in wM2 and tjM2/ALM. An early excitatory response in PPC and a transient suppression of firing in tjM1 also appeared across learning (non-parametric permutation test). Firing rates of all areas in Novice mice returned to baseline levels shortly after whisker stimulation, whereas in Expert mice wS2, PPC, DLS, wM2, tjM2/ALM and tjM1 neurons showed increased activity in different parts of the delay. PPC neuronal firing remained elevated only during the first part of the delay period, returning to baseline before the auditory cue, while the activity of wM2, Striatum and tjM1 neurons ramped up towards the lick onset. On average neurons in tjM2/ALM maintained elevated firing throughout the entire delay period. These results suggest that the whisker training enhanced the initial distributed processing of whisker stimulus, and formed the memory of a licking motor plan among higher-order areas of whisker and tongue/jaw motor cortex.

We further investigated how selectively those neurons were recruited for task execution by considering other trial types. First, we found that the delay period activities were absent in Miss trials (Figure S4B-C). Second, we quantified response selectivity of individual neurons for Hit and Correct-rejection trials based on ROC analysis (Figure 3E; see STAR Methods), and found in most areas that a larger population of neurons became selectively recruited during the delay period comparing Expert and Novice mice. These results suggest the involvement of the acquired neuronal delay period activity in correct whisker detection and delayed-licking. Silicon probe recordings thus provide consistent and complementary information to wide-field calcium imaging.

Stable and acquired patterns of neuronal firing

The overall population activity patterns in different brain areas were thus profoundly different (Figures 2 and 3), but even neurons recorded from the same silicon probe could show striking diversity. Assuming that neurons with similar firing dynamics perform similar processing, it is informative to identify those temporal patterns and investigate whether a single pattern is confined or distributed across the brain. We therefore performed clustering of neurons according to their temporal firing pattern in four trial types (Hit, Miss, Correct-rejection and False-alarm) using an unsupervised approach (Figures 4 and S5; see STAR Methods). Gaussian mixture model (GMM) clustering after dimensionality reduction with PCA and spectral embedding (Figure S5A-B) yielded 24 clusters of neurons, which were sorted by their onset latency (Figure 4A) (Hastie et al., 2009).

In agreement with the observation of profound changes during the delay period after whisker training (Figures 1-3), neuronal clustering delineated several whisker responsive clusters with distinct temporal dynamics (Figure 4A, clusters C2-C7). The clusters that showed an initial, sharp firing (C2-C4) were distributed across wS1, wS2, wM1, wM2 and DLS and were derived from both Novice and Expert mice (Figures 4A-C, and S5C). On the contrary, Expert neurons were preponderant in all delay responsive clusters (C5-C7) (Figures 4A-C and S5C). Among them, C5 with transient early-delay firing and C7 with inhibitory delay response, both derived from diverse motor-related or higher-order areas; C6, showing persistent excitatory activity lasting until the end of delay, comprising predominantly tjM2/ALM and wM2 neurons. Lick-related clusters (C13-15, C17-19) were distributed among tjM1, tjM2/ALM, wM2 and DLS, with partial ramping-up activity reflecting pre-licking signals towards the end of delay (Figures 4A-D and S5C). The lick-related clusters may also contribute to signalling reward expectation. For some areas the dominant cluster changed between Expert and Novice mice. Similar activity patterns dominated visual, whisker and auditory sensory areas before and after whisker training while novel patterns emerged in higher-order (PPC, dCA1, mPFC) and motor related regions (wM1, wM2, tjM1, tjM2/ALM) (Figures 4D and S5D). These results suggest that the processing of whisker stimulus during the delay period was initially confined in whisker sensorimotor areas, then widely distributed, and finally converged in the frontal areas for whisker, tongue/jaw and DLS to plan licking.

Focalized delay period activity in frontal cortex

The most prominent cortical change after whisker training was the emergence of wide-spread delay period activity patterns at the level of population and single neurons (Figures 2C, 3B-E, 4). In the late delay period, Expert mice showed uninstructed, anticipatory movements of whisker, jaw and tongue (Figures 1E-F, S1C-D), which could be broadly correlated with activity across the brain (Musall et al., 2019; Steinmetz et al., 2019). To identify neural activities more directly related to the task execution, we leveraged trial-by-trial variability of the neuronal activity and anticipatory movements (Figure 5).

First, we separated neural activities by selecting "Quiet" trials in which mice did not make jaw movements during the delay period (Figures 5A-B, S6A; see STAR Methods). When only Quiet trials were considered, the wide-spread calcium activity during the delay, observed in the average of all trials, became more localized to wM2 and tjM2/ALM (Figure 5A). This focal activation together with deactivation of orofacial sensorimotor areas emerged by learning (threshold $p<0.05$, Wilcoxon rank-sum test, FDR-corrected). Electrophysiology data also demonstrated a consistent localization of the neuronal delay period activity (Figure 5B). In Quiet Hit trials, only tjM2/ALM population firing remained elevated throughout the delay period and was clearly enhanced by whisker training (non-parametric permutation test). In the other regions, the whisker-evoked firing returned to baseline just as in Novice mice. Thus, selecting Quiet trials demonstrated that the essential processing in cortex during the delay period is localized in a focal frontal region including tjM2/ALM.

Assessing the impact of movements considering only Quiet trials highlighted the unique role of tjM2/ALM during the delay period. However, Quiet Hits represented a minority of all Hit trials in Expert mice (42 ± 2 %; mean ± SEM). Trials with movements during the delay period may carry richer information about how neuronal activity drives behavior. Therefore, to capture neuronal encoding during single trials, we next took a generalized linear model (GLM) approach (Nelder and Wedderburn, 1972) and fitted a Poisson encoding model to spiking data of individual neurons including all correct trials (Park et al., 2014) (Figures 5C-E and S6B-F; see STAR Methods). Three types of model predictors were included (Figure S6B): discrete task events (e.g. sequential boxcars time-locked to sensory stimuli and first lick onset); analog movement signals (whisker, tongue and jaw speed); and slow variables capturing motivational factors (e.g. current trial number) and trial history (e.g. outcome of the previous trial). We assessed fit quality using predictor-spike mutual information (MI) and only considered neurons with good quality of fit for the rest of analysis (Cover and Thomas, 1991; Gerstner et al., 2014) (Figure S6E, see STAR Methods). The contribution of each model variable to the neuron's spiking activity was tested by re-fitting the data after excluding the variable of interest (reduced model) and comparing the fit quality to the model including all variables (full model) using a likelihood ratio test (Figures 5C and S6D) (Buse, 1982).

Whisker sensorimotor areas (wS1, wS2, wM1 and wM2), in both Novice and Expert mice, had the largest proportion of neurons significantly modulated by whisker stimulus in the first 100 ms (Whisker encoding neurons, Figure 5C top). Among these areas, the fraction of Whisker encoding neurons only increased across whisker training in wM2 (p=0.032, Pearson’s chi-square test), while it decreased in wS2 (p=0.029) and wM1 (p=0.014). In contrast, Delay encoding neurons that were significantly modulated between 100 ms and 1 s after the whisker stimulus (Figure 5C, middle) were mainly found in tjM2/ALM, but also in wM2, which was strikingly enhanced by whisker training ($p<10^{-5}$). Some neurons in wM2, tjM2/ALM, tjM1 and DLS were found to be significantly modulated during the 200 ms prior to the lick onset before and after whisker training (Figure 5C; PreLick encoding neurons) reflecting the licking initiation signal in these areas beyond those captured by orofacial movements or sound onset predictors in the model. We then asked whether similar populations of neurons encode different task variables in each area (Figure 5D). To address this question, we quantified the degree of overlap across populations of Whisker, Delay and PreLick encoding neurons in the key areas of interest and visualized it using Venn diagrams (Figure 5D). We found that enhanced Delay and Prelick encoding populations were largely non-overlapping. Finally, we asked whether our encoding model, fitted using all trials, can reproduce neuronal activity in Quiet trials (Figure 5E). Model-reconstructed PSTHs after removing movement-related regressors confirmed that neurons in tjM2/ALM kept their firing throughout the delay period, while the firing in other areas returned to baseline, in agreement with the empirical data. This result supports the model validity and highlights the prominence of tjM2/ALM.

Routing of whisker information to frontal cortex

tjM2/ALM appears to be the most important processing node during the delay period, even persisting in Quiet trials (Figure 5A-B) and after accounting for preparatory movements (Figure 5C-D). However, neuronal activity diverges between Novice vs

Expert and between Hit vs Miss trials at a very early phase of the delay period (Figures 2, 3, S2 and S4) suggesting this as a critical window for decision making. We therefore investigated early neuronal delay period activity by tracking the cortical pathway that signals whisker input to tjM2/ALM by following the rapid sequence of the whisker-evoked responses among anatomically connected regions (Figure 6). Frame-by-frame analysis of high-speed calcium imaging data showed that the whisker stimulus evoked the earliest responses in wS1 at 20 ms after the stimulus onset; activity then spread to wS2, wM1, wM2, Aud, PPC, retrosplenial area and finally reached tjM2/ALM (Figures 6A and S7A). This earliest sequence including the deactivation of tjM1/S1 was significantly enhanced by whisker training (Figure 6A, threshold $p<0.05$ by Wilcoxon rank-sum test, FDR-corrected), but was diminished when mice failed to lick (Figure S7C-D, threshold $p<0.05$ by Wilcoxon rank-sum test, FDR-corrected), indicating its possible involvement in whisker-detection and delayed-licking. Neuronal firing showed a consistent spatiotemporal pattern of the whisker-evoked sequence, including a suppression of firing in tjM1 and its enhancement by whisker training (Figure S7B). Sorting population responses in different areas according to latency, revealed a clear sequential development of firing within 100 ms from wS1 to tjM2/ALM (Figure 6B) which was mostly conserved between Novice and Expert. However, the single neuron latency in wM1 was delayed, whereas it was shortened in wM2 after whisker training (Figure 6C, wM1: $p=0.008$, wM2: $p=0.041$, Wilcoxon rank-sum test, FDR-corrected). Moreover, among all areas recorded, wM2 showed the earliest significant increase in firing upon whisker training, as well as the earliest significant difference comparing Hit and Miss trials (Figure 6D, Novice vs Expert: $p= 0.022$, Hit vs Miss: $p=0.025$, non-parametric permutation test, FDR-corrected). Altogether, these results highlight the role of wM2 as a potential node to bridge sensory to motor activity by relaying whisker sensory information from wS1/wS2 to tjM2/ALM.

Temporally-specific causal contributions of different brain regions

Imaging and electrophysiology data suggested multiple phases of neural processing for whisker-detection, motor planning and delayed-licking. To examine the causal contribution of brain regions in each of these phases, we performed spatiotemporally-selective optogenetic inhibition (Figure 7A). In transgenic mice expressing ChR2 in GABAergic neurons (n=9, VGAT-ChR2) (Guo et al., 2014), we applied blue light pulses to each brain region through an optical fiber. The blue light was delivered randomly in one-third of the trials, occurring in one of the four temporal windows: Baseline (from visual cue onset to 100 ms before whisker stimulus onset), Whisker (from 100 ms before to 200 ms after whisker stimulus onset), Delay (from 200 ms to 1000 ms after whisker stimulus onset), or Response (from 0 ms to 1100 ms after auditory cue onset).

Inhibition in different time windows provided spatial maps of the behavioral impact (Figures 7 and S8). During the Baseline window, a decrease in Hit rate occurred after inactivation of a few regions, including dCA1 and mPFC (Light-off versus Light, dCA1, *p*=0.016, mPFC, *p*=0.031; Wilcoxon signed-rank test, corrected for multiple comparison). During the Whisker window, a decrease in Hit rate occurred in many regions with the strongest impact in wS2 (Light-off versus Light, *p*=0.016, Wilcoxon signed-rank test, corrected for multiple comparison). In this window, False-alarm rate increased upon inhibition of frontal areas. In contrast, during the Delay period, inhibition of tjM2/ALM and mPFC produced a strong reduction in Hit rate (Light-off versus Light trials: tjM2/ALM, *p*=0.016; mPFC, *p*=0.016, Wilcoxon signed-rank test, corrected for multiple comparison). The strongest increase in False-alarm rate occurred for inhibition of wM2 and dCA1, in this epoch. Finally, during the Response window, when the licking behavior had to be executed, inhibition of tongue-related tjM1 and tjM2/ALM, but also whisker-related wM2, impaired behavior by decreasing both Hit and False-alarm rate (Light-off versus Light, tjM1, p=0.016; tjM2/ALM, p=0.016; wM2, p=0.016, Wilcoxon signed-rank test, corrected for multiple comparison), supporting the causal involvement of the acquired pre-lick firing of wM2 neurons (Figure 5C). The differential impact of inactivating nearby cortical regions is consistent with high spatiotemporal specificity of our optogenetic manipulations. Thus, spatiotemporal mapping of causal impacts suggested that critical whisker processing was initially distributed across diverse cortical regions, and then converged in frontal regions for planning lick motor output, in agreement with neural activity data.

If a brain region is critically involved in task execution, neural activity in that area would code behavioral decision, and its inhibition would cause behavioral impairments.

To further evaluate the correlation between selective neuronal firing and its causal contribution to behavior, we defined an involvement index for each area and time window as the product of the difference in firing rate between Hit versus Correct-rejection and the change in Hit rate upon optogenetic inhibition (Figure 8A). The involvement index during the Whisker period was largest in wS2 and wS1 (wS2 and wS1 versus other areas, $p<0.01$, non-parametric permutation test) highlighting these areas as the main nodes of whisker sensory processing. During the Delay period, tjM2/ALM had the largest involvement index (tjM2/ALM versus other areas, $p<0.001$, non-parametric permutation test). The most critical area in the Response window was tjM1 (tjM1 versus other areas, $p<0.05$, non-parametric permutation test).

DISCUSSION

We found converging evidence for the temporally distinct involvement of diverse cortical regions in delayed sensorimotor transformation using five comprehensive and complementary technical approaches: i) a two-step learning paradigm to differentiate specific computations acquired for converting a sensory stimulus to a motor plan, ii) high-speed video filming of orofacial movements to account for movement related neuronal activity during the delay, iii) high-speed wide-field optical calcium imaging, iv) cortex-wide silicon probe single-neuron recordings, and v) task epoch- and area-specific optogenetic inactivation. Our analyses focused on learning-induced changes in causal neural activity transforming whisker-deflection evoked sensory responses into delay period activity for motor planning, leading to a specific hypothesis for the underlying neuronal circuit mechanisms discussed below.

Localized preparatory neuronal activity in frontal cortex

In the present delayed-response task, mice learned to detect a brief whisker deflection and lick a water spout after one second. Broad regions of cortex showed elevated activity in Expert mice during parts of the delay period in Hit trials (Figures 2 and 3). By clustering neuronal firing patterns, we found that delay-period responsive neurons (cluster C6) were found predominantly in tjM2/ALM, as well as wM2, wM1 and DLS

(Figures 4 and S5). However, rigorous behavioral analysis showed that delayed-lick learning was accompanied by emergence of preparatory orofacial movements during the delay period (Figure 1). The orofacial movements during the delay period increased through learning specifically in Hit trials (Figures 1E-F and S1C-D), suggesting that those movements may contribute a form of embodied sensorimotor memory in which ongoing movements help maintain a plan for delayed licking (Mayrhofer et al., 2019), possibly present in many similar delayed-response tasks. At the same time, we also found that large parts of the spiking activity in many regions were correlated with orofacial movements (Table S1), in agreement with previous studies which reported that movement was accompanied by changes in brain states (Crochet and Petersen, 2006; McGinley et al., 2015) and sensory processing (Crochet and Petersen, 2006; Ferezou et al., 2007) with broad impact across cortical areas (Fernandez et al., 2017; Gilad et al., 2018; Musall et al., 2019; Stringer et al., 2019). When only trials free of such preparatory movements during the delay period were analyzed, wide-field imaging and electrophysiology demonstrated a localized excitatory activity in a small region of secondary motor area including tjM2/ALM (Figure 5A-B). Trial-by-trial analysis of all trials, by accounting for movement contributions using linear regression, further confirmed that delay period-responsive neurons were highly localized in tjM2/ALM (Figures 5C-E). Finally, inactivation of tjM2/ALM during the delay period prominently disrupted task execution in expert mice (Figure 7). On the other hand, given that there is no task-related neuronal delay activity in tjM2/ALM of Novice mice (Figures 2-5), it is unlikely that this region is important during the delay period in Novice mice. Our study thus confirms and further extends previous studies demonstrating the critical role of ALM in motor planning in delayed-response tasks (Guo et al., 2014; Li et al., 2015).

Lick and No-Lick signals in tjM1

In Expert mice, we found that the whisker stimulus evoked a sharp deactivation broadly across orofacial sensorimotor cortex including tjM1, an area thought to be involved in the initiation of licking (Figures 2, 3, 5 and 6) (Mayrhofer et al., 2019). This deactivation remained prominent throughout the delay in Quiet trials (Figure 5). In a previous study

(Mayrhofer et al., 2019), such deactivation in tjM1 was not observed in a whisker detection task without a delay period, where tjM1 neurons were activated soon after a whisker deflection. One interesting possibility is thus that the deactivation in tjM1 develops through learning of a task where suppression of immediate licking is demanded. Previous studies in human subjects have suggested the importance of such inhibitory mechanisms for preventing actions from being emitted inappropriately (Chikazoe et al., 2009; Duque et al., 2017). Thus, parallel inhibitory and excitatory delay period components might be common principles of response preparation preserved across species (Cohen et al., 2010).

During the response window, neural clustering determined most lick related neurons in tjM1 (C13-15 and C17). Consistent with this and previous findings (Mayrhofer et al., 2019), optogenetic inhibition of tjM1 resulted in strongest suppression of licking suggesting the importance of this area in lick initiation (Figure 7 and 8A) and highlighting the functional and causal distinctions between nearby frontal regions.

Initiation of persistent activity by wM2

In the present behavioral paradigm, learning the relevance of the C2 whisker was the critical step for mice. The well-controlled sensory stimulus allowed the step-by-step investigation of sensory propagation. The earliest cortical response to whisker stimulus occurred in wS1 and wS2, which changed relatively little across whisker training (Figures 2, 3 and 6). This initial processing is causally essential as shown by optogenetic inactivation (Figure 7A), and therefore wS1 and wS2 appear to form the cortical starting point of whisker sensory processing for the present task, in agreement with previous studies (Kwon et al., 2016; Kyriakatos et al., 2017; Le Merre et al., 2018; Mayrhofer et al., 2019; Miyashita and Feldman, 2013; Sachidhanandam et al., 2013; Yang et al., 2016).

This early delay window after the whisker stimulus seems to be the critical period for decision making and when the whisker information is converted to preparatory neuronal activity in Hit but not Miss trials (Figures S4 and 6). Within this period, wM2 showed the earliest significant increase in whisker-evoked firing (< 50 ms) in both Novice *vs* Expert and Hit *vs* Miss comparisons (Figure 6). Thus, wM2 might serve as a key node in the corticocortical network to begin the process of converting a whisker sensory stimulus into longer-lasting preparatory neuronal activity. Shortly after wM2 activation, tjM2/ALM, an important premotor area for control of licking (Guo et al., 2014; Li et al., 2015; Mayrhofer et al., 2019), started to increase firing (Figure 6). Through cortico-cortical connectivity (Luo et al., 2019), activity in wM2 could contribute directly to exciting the neighboring region tjM2/ALM, which manifested the most prominent delay period activity through whisker training (Figures 4 and 5), consistent with previous studies (Chen et al., 2017; Li et al., 2015).

A cortico-cortical network for learned sensorimotor planning

Our results suggest a hypothesis for a minimal cortical network connecting whisker sensory coding to preparatory neuronal activity for motor planning: a pathway wS1 -> wS2 -> wM2 -> tjM2/ALM could be the main stream of signal processing (Figure 8B). Some of the most prominent whisker-related changes through whisker training occurred in wM2 and tjM2/ALM, and it is possible that reward-related potentiation of synaptic transmission between wS2 -> wM2 and wM2 -> tjM2/ALM could underlie important aspects of the present learning paradigm. All of these cortical areas are likely to be connected through reciprocal excitatory long-range axonal projections, which could give rise to recurrent excitation helping to prolong firing rates of neurons in relevant brain regions during the delay period of Hit trials. Enhanced reciprocal excitatory connectivity amongst wS1 <-> wS2 <-> wM2 <-> tjM2/ALM could be mediated by Hebbian types of synaptic plasticity. Interestingly, in a related whisker detection task without a delay period, enhanced reciprocal signaling between wS1 and wS2 has already been proposed to play an important role (Kwon et al., 2016; Yamashita and Petersen, 2016). It is also important to note that a large number of subcortical structures are also likely to be involved in task performance including thalamus (El-Boustani et al., 2020; Guo et al., 2017), basal ganglia (Sippy et al., 2015) and cerebellum (Chabrol et al., 2019; Gao et al., 2018).

In summary, here, we found evidence that learning induces a highly-dynamic initial spread of sensory processing across cortical areas followed by a convergence of activity supporting a motor plan in a localized region of frontal cortex, and we propose the causal contribution of a specific cortico-cortical circuit, which we hypothesize could be strengthened across learning by reward-driven synaptic plasticity.

Acknowledgments

We thank Fritjof Helmchen for TIGRE1.0-RCaMP mice, Eloise Charrière for management of mouse colonies and help with behavioral training, Sai Krishna Teja Sadhu for help with image analysis, and Flavio Martinelli for help with video-tracking. This work was supported by the Swiss National Science Foundation (310030B_166595, 31003A_182010 and CRSII5_177237 to CCHP, 200020_165538 to SPM) and the European Research Council (ERC-2011-ADG 293660) to CCHP, European Union’s Marie Skłodowska-Curie Actions (665667, 798617), the Research Foundation for Opto-science and Technology, the Brain Science Foundation, the Japan Society for the Promotion of Sciences, and the Ichiro Kanehara Foundation to KT.

Author Contributions

VE, KT, SC and CCHP conceptualized the study; VE and KT developed neural and behavioral experiment setups; VE, KT, and MB obtained neural and behavioral data; VE, KT, ABL and AO obtained histological data; GF and YL built the two-photon tomography system; VE, KT, SPM and AM analyzed the data; VE, KT, SC and CCHP wrote the manuscript; all authors discussed and edited the manuscript; and CCHP provided overall supervision.

Declaration of Interests

The authors declare no competing interests.

REFERENCES

Abbe, E. (2017). Community detection and stochastic block models: recent developments. J. Mach. Learn. Res. *18*, 6446–6531.

Allen, W.E., Kauvar, I.V., Chen, M.Z., Richman, E.B., Yang, S.J., Chan, K., Gradinaru, V., Deverman, B.E., Luo, L., and Deisseroth, K. (2017). Global Representations of Goal-Directed Behavior in Distinct Cell Types of Mouse Neocortex. Neuron *94*, 891-907.e6.

Andermann, M.L., Kerlin, A.M., Roumis, D.K., Glickfeld, L.L., and Reid, R.C. (2011). Functional specialization of mouse higher visual cortical areas. Neuron *72*, 1025–1039.

Benjamini, Y., and Hochberg, Y. (1995). Controlling the False Discovery Rate: A Practical and Powerful Approach to Multiple Testing. J. R. Stat. Soc. Ser. B Methodol. *57*, 289–300.

Bethge, P., Carta, S., Lorenzo, D.A., Egolf, L., Goniotaki, D., Madisen, L., Voigt, F.F., Chen, J.L., Schneider, B., Ohkura, M., et al. (2017). An R-CaMP1.07 reporter mouse for cell-type-specific expression of a sensitive red fluorescent calcium indicator. PloS One *12*, e0179460.

Bosman, L.W.J., Houweling, A.R., Owens, C.B., Tanke, N., Shevchouk, O.T., Rahmati, N., Teunissen, W.H.T., Ju, C., Gong, W., Koekkoek, S.K.E., et al. (2011). Anatomical pathways involved in generating and sensing rhythmic whisker movements. Front. Integr. Neurosci. *5*, 53.

Buse, A. (1982). The likelihood ratio, Wald, and Lagrange multiplier tests: An expository note. Am. Stat. *36*, 153–157.

Buzsáki, G. (2004). Large-scale recording of neuronal ensembles. Nat. Neurosci. *7*, 446–451.

Carandini, M., and Churchland, A.K. (2013). Probing perceptual decisions in rodents. Nat. Neurosci. *16*, 824–831.

Chabrol, F.P., Blot, A., and Mrsic-Flogel, T.D. (2019). Cerebellar Contribution to Preparatory Activity in Motor Neocortex. Neuron *103*, 506-519.e4.

Chen, T.-W., Li, N., Daie, K., and Svoboda, K. (2017). A Map of Anticipatory Activity in Mouse Motor Cortex. Neuron *94*, 866-879.e4.

Chikazoe, J., Jimura, K., Hirose, S., Yamashita, K., Miyashita, Y., and Konishi, S. (2009). Preparation to inhibit a response complements response inhibition during performance of a stop-signal task. J. Neurosci. Off. J. Soc. Neurosci. *29*, 15870–15877.

Cohen, O., Sherman, E., Zinger, N., Perlmutter, S., and Prut, Y. (2010). Getting ready to move: transmitted information in the corticospinal pathway during preparation for movement. Curr. Opin. Neurobiol. *20*, 696–703.

Cover, T.M., and Thomas, J.A. (1991). Entropy, relative entropy and mutual information. Elem. Inf. Theory *2*, 1–55.

Crochet, S., and Petersen, C.C.H. (2006). Correlating whisker behavior with membrane potential in barrel cortex of awake mice. Nat. Neurosci. *9*, 608–610.

Cunningham, J.P., Byron, M.Y., Shenoy, K.V., and Sahani, M. (2008). Inferring neural firing rates from spike trains using Gaussian processes. In Advances in Neural Information Processing Systems, pp. 329–336.

Diamond, M.E., and Arabzadeh, E. (2013). Whisker sensory system – From receptor to decision. Prog. Neurobiol. *103*, 28–40.

Diamond, M.E., von Heimendahl, M., Knutsen, P.M., Kleinfeld, D., and Ahissar, E. (2008). “Where” and “what” in the whisker sensorimotor system. Nat. Rev. Neurosci. *9*, 601–612.

Duque, J., Greenhouse, I., Labruna, L., and Ivry, R.B. (2017). Physiological Markers of Motor Inhibition during Human Behavior. Trends Neurosci. *40*, 219–236.

El-Boustani, S., Sermet, B.S., Foustoukos, G., Oram, T.B., Yizhar, O., and Petersen, C.C.H. (2020). Anatomically and functionally distinct thalamocortical inputs to primary and secondary mouse whisker somatosensory cortices. Nat. Commun. *11*, 3342.

Engelhard, B., Finkelstein, J., Cox, J., Fleming, W., Jang, H.J., Ornelas, S., Koay, S.A., Thiberge, S.Y., Daw, N.D., and Tank, D.W. (2019). Specialized coding of sensory, motor and cognitive variables in VTA dopamine neurons. Nature *570*, 509–513.

Erlich, J.C., Bialek, M., and Brody, C.D. (2011). A cortical substrate for memory-guided orienting in the rat. Neuron *72*, 330–343.

Esmaeili, V., and Diamond, M.E. (2019). Neuronal Correlates of Tactile Working Memory in Prefrontal and Vibrissal Somatosensory Cortex. Cell Rep. *27*, 3167-3181.e5.

Fassihi, A., Akrami, A., Pulecchi, F., Schönfelder, V., and Diamond, M.E. (2017). Transformation of Perception from Sensory to Motor Cortex. Curr. Biol. CB *27*, 1585-1596.e6.

Feldmeyer, D., Brecht, M., Helmchen, F., Petersen, C.C.H., Poulet, J.F.A., Staiger, J.F., Luhmann, H.J., and Schwarz, C. (2013). Barrel cortex function. Prog. Neurobiol. *103*, 3–27.

Ferezou, I., Haiss, F., Gentet, L.J., Aronoff, R., Weber, B., and Petersen, C.C.H. (2007). Spatiotemporal dynamics of cortical sensorimotor integration in behaving mice. Neuron *56*, 907–923.

Fernandez, L.M.J., Comte, J.-C., Le Merre, P., Lin, J.-S., Salin, P.-A., and Crochet, S. (2017). Highly Dynamic Spatiotemporal Organization of Low-Frequency Activities During Behavioral States in the Mouse Cerebral Cortex. Cereb. Cortex N. Y. N 1991 *27*, 5444–5462.

Funahashi, S., Bruce, C.J., and Goldman-Rakic, P.S. (1989). Mnemonic coding of visual space in the monkey’s dorsolateral prefrontal cortex. J. Neurophysiol. *61*, 331–349.

Fuster, J.M., and Alexander, G.E. (1971). Neuron activity related to short-term memory. Science *173*, 652–654.

Gao, Z., Davis, C., Thomas, A.M., Economo, M.N., Abrego, A.M., Svoboda, K., De Zeeuw, C.I., and Li, N. (2018). A cortico-cerebellar loop for motor planning. Nature *563*, 113–116.

Gerstner, W., Kistler, W.M., Naud, R., and Paninski, L. (2014). Neuronal dynamics: From single neurons to networks and models of cognition (Cambridge University Press).

Gilad, A., Gallero-Salas, Y., Groos, D., and Helmchen, F. (2018). Behavioral Strategy Determines Frontal or Posterior Location of Short-Term Memory in Neocortex. Neuron *99*, 814-828.e7.

Gong, S., Doughty, M., Harbaugh, C.R., Cummins, A., Hatten, M.E., Heintz, N., and Gerfen, C.R. (2007). Targeting Cre Recombinase to Specific Neuron Populations with Bacterial Artificial Chromosome Constructs. J. Neurosci. *27*, 9817.

Gorski, J.A., Talley, T., Qiu, M., Puelles, L., Rubenstein, J.L.R., and Jones, K.R. (2002). Cortical Excitatory Neurons and Glia, But Not GABAergic Neurons, Are Produced in the Emx1-Expressing Lineage. J. Neurosci. *22*, 6309.

Guo, Z.V., Li, N., Huber, D., Ophir, E., Gutnisky, D., Ting, J.T., Feng, G., and Svoboda, K. (2014). Flow of cortical activity underlying a tactile decision in mice. Neuron *81*, 179–194.

Guo, Z.V., Inagaki, H.K., Daie, K., Druckmann, S., Gerfen, C.R., and Svoboda, K. (2017). Maintenance of persistent activity in a frontal thalamocortical loop. Nature *545*, 181–186.

Han, Y., Kebschull, J.M., Campbell, R.A.A., Cowan, D., Imhof, F., Zador, A.M., and Mrsic-Flogel, T.D. (2018). The logic of single-cell projections from visual cortex. Nature *556*, 51–56.

Harvey, C.D., Coen, P., and Tank, D.W. (2012). Choice-specific sequences in parietal cortex during a virtual-navigation decision task. Nature *484*, 62–68.

Hastie, T., Tibshirani, R., and Friedman, J. (2009). The elements of statistical learning: data mining, inference, and prediction (Springer Science & Business Media).

Hattori, R., Danskin, B., Babic, Z., Mlynaryk, N., and Komiyama, T. (2019). Area-Specificity and Plasticity of History-Dependent Value Coding During Learning. Cell *177*, 1858-1872.e15.

Hong, Y.K., Lacefield, C.O., Rodgers, C.C., and Bruno, R.M. (2018). Sensation, movement and learning in the absence of barrel cortex. Nature *561*, 542–546.

Hutson, K.A., and Masterton, R.B. (1986). The sensory contribution of a single vibrissa's cortical barrel. J. Neurophysiol. *56*, 1196–1223.

Kwon, S.E., Yang, H., Minamisawa, G., and O'Connor, D.H. (2016). Sensory and decision-related activity propagate in a cortical feedback loop during touch perception. Nat. Neurosci. *19*, 1243–1249.

Kyriakatos, A., Sadashivaiah, V., Zhang, Y., Motta, A., Auffret, M., and Petersen, C.C.H. (2017). Voltage-sensitive dye imaging of mouse neocortex during a whisker detection task. Neurophotonics *4*, 031204.

de Lafuente, V., and Romo, R. (2006). Neural correlate of subjective sensory experience gradually builds up across cortical areas. Proc. Natl. Acad. Sci. U. S. A. *103*, 14266–14271.

Le Merre, P., Esmaeili, V., Charrière, E., Galan, K., Salin, P.-A., Petersen, C.C.H., and Crochet, S. (2018). Reward-Based Learning Drives Rapid Sensory Signals in Medial Prefrontal Cortex and Dorsal Hippocampus Necessary for Goal-Directed Behavior. Neuron *97*, 83-91.e5.

Lein, E.S., Hawrylycz, M.J., Ao, N., Ayres, M., Bensinger, A., Bernard, A., Boe, A.F., Boguski, M.S., Brockway, K.S., Byrnes, E.J., et al. (2007). Genome-wide atlas of gene expression in the adult mouse brain. Nature *445*, 168–176.

Li, N., Chen, T.-W., Guo, Z.V., Gerfen, C.R., and Svoboda, K. (2015). A motor cortex circuit for motor planning and movement. Nature *519*, 51–56.

Luo, L., Callaway, E.M., and Svoboda, K. (2018). Genetic Dissection of Neural Circuits: A Decade of Progress. Neuron *98*, 256–281.

Luo, P., Li, A., Zheng, Y., Han, Y., Tian, J., Xu, Z., Gong, H., and Li, X. (2019). Whole Brain Mapping of Long-Range Direct Input to Glutamatergic and GABAergic Neurons in Motor Cortex. Front. Neuroanat. *13*, 44.

MacDowell, C.J., and Buschman, T.J. (2020). Low-Dimensional Spatiotemporal Dynamics Underlie Cortex-wide Neural Activity. Curr. Biol.

Macosko, E.Z., Basu, A., Satija, R., Nemesh, J., Shekhar, K., Goldman, M., Tirosh, I., Bialas, A.R., Kamitaki, N., and Martersteck, E.M. (2015). Highly parallel genome-wide expression profiling of individual cells using nanoliter droplets. Cell *161*, 1202–1214.

Madisen, L., Zwingman, T.A., Sunkin, S.M., Oh, S.W., Zariwala, H.A., Gu, H., Ng, L.L., Palmiter, R.D., Hawrylycz, M.J., Jones, A.R., et al. (2010). A robust and high-throughput Cre reporting and characterization system for the whole mouse brain. Nat. Neurosci. *13*, 133–140.

Makino, H., Ren, C., Liu, H., Kim, A.N., Kondapaneni, N., Liu, X., Kuzum, D., and Komiyama, T. (2017). Transformation of Cortex-wide Emergent Properties during Motor Learning. Neuron *94*, 880-890.e8.

Marshel, J.H., Garrett, M.E., Nauhaus, I., and Callaway, E.M. (2011). Functional specialization of seven mouse visual cortical areas. Neuron *72*, 1040–1054.

Mayford, M., Bach, M.E., Huang, Y.Y., Wang, L., Hawkins, R.D., and Kandel, E.R. (1996). Control of memory formation through regulated expression of a CaMKII transgene. Science *274*, 1678–1683.

Mayrhofer, J.M., El-Boustani, S., Foustoukos, G., Auffret, M., Tamura, K., and Petersen, C.C.H. (2019). Distinct Contributions of Whisker Sensory Cortex and Tongue-Jaw Motor Cortex in a Goal-Directed Sensorimotor Transformation. Neuron *103*, 1034-1043.e5.

McGinley, M.J., Vinck, M., Reimer, J., Batista-Brito, R., Zagha, E., Cadwell, C.R., Tolias, A.S., Cardin, J.A., and McCormick, D.A. (2015). Waking State: Rapid Variations Modulate Neural and Behavioral Responses. Neuron *87*, 1143–1161.

Miyashita, T., and Feldman, D.E. (2013). Behavioral detection of passive whisker stimuli requires somatosensory cortex. Cereb. Cortex N. Y. N 1991 *23*, 1655–1662.

Musall, S., Kaufman, M.T., Juavinett, A.L., Gluf, S., and Churchland, A.K. (2019). Single-trial neural dynamics are dominated by richly varied movements. Nat. Neurosci. *22*, 1677–1686.

Nelder, J.A., and Wedderburn, R.W.M. (1972). Generalized Linear Models. J. R. Stat. Soc. Ser. Gen. *135*, 370–384.

Park, I.M., Meister, M.L.R., Huk, A.C., and Pillow, J.W. (2014). Encoding and decoding in parietal cortex during sensorimotor decision-making. Nat. Neurosci. *17*, 1395–1403.

Paxinos, G., and Franklin, K.B. (2019). Paxinos and Franklin's the mouse brain in stereotaxic coordinates (Academic press).

Petersen, C.C.H. (2019). Sensorimotor processing in the rodent barrel cortex. Nat. Rev. Neurosci. *20*, 533–546.

Pinto, L., Rajan, K., DePasquale, B., Thiberge, S.Y., Tank, D.W., and Brody, C.D. (2019). Task-Dependent Changes in the Large-Scale Dynamics and Necessity of Cortical Regions. Neuron *104*, 810-824.e9.

Rossant, C., Kadir, S.N., Goodman, D.F.M., Schulman, J., Hunter, M.L.D., Saleem, A.B., Grosmark, A., Belluscio, M., Denfield, G.H., Ecker, A.S., et al. (2016). Spike sorting for large, dense electrode arrays. Nat. Neurosci. *19*, 634–641.

Sachidhanandam, S., Sreenivasan, V., Kyriakatos, A., Kremer, Y., and Petersen, C.C.H. (2013). Membrane potential correlates of sensory perception in mouse barrel cortex. Nat. Neurosci. *16*, 1671–1677.

Shamash, P., Carandini, M., Harris, K., and Steinmetz, N. (2018). A tool for analyzing electrode tracks from slice histology. BioRxiv 447995.

Sippy, T., Lapray, D., Crochet, S., and Petersen, C.C.H. (2015). Cell-Type-Specific Sensorimotor Processing in Striatal Projection Neurons during Goal-Directed Behavior. Neuron *88*, 298–305.

Soleimanzad Haleh, Gurden Hirac, and Pain Frédéric (2017). Optical properties of mice skull bone in the 455- to 705-nm range. J. Biomed. Opt. *22*, 1–4.

Sreenivasan, V., Esmaeili, V., Kiritani, T., Galan, K., Crochet, S., and Petersen, C.C.H. (2016). Movement Initiation Signals in Mouse Whisker Motor Cortex. Neuron *92*, 1368–1382.

Steinmetz, N.A., Zatka-Haas, P., Carandini, M., and Harris, K.D. (2019). Distributed coding of choice, action and engagement across the mouse brain. Nature *576*, 266–273.

Stringer, C., Pachitariu, M., Steinmetz, N., Reddy, C.B., Carandini, M., and Harris, K.D. (2019). Spontaneous behaviors drive multidimensional, brainwide activity. Science *364*, 255.

Taniguchi, H., He, M., Wu, P., Kim, S., Paik, R., Sugino, K., Kvitsiani, D., Kvitsani, D., Fu, Y., Lu, J., et al. (2011). A resource of Cre driver lines for genetic targeting of GABAergic neurons in cerebral cortex. Neuron *71*, 995–1013.

Tanji, J., and Evarts, E.V. (1976). Anticipatory activity of motor cortex neurons in relation to direction of an intended movement. J. Neurophysiol. *39*, 1062–1068.

Vanni, M.P., Chan, A.W., Balbi, M., Silasi, G., and Murphy, T.H. (2017). Mesoscale Mapping of Mouse Cortex Reveals Frequency-Dependent Cycling between Distinct Macroscale Functional Modules. J. Neurosci. Off. J. Soc. Neurosci. *37*, 7513–7533.

Von Luxburg, U. (2007). A tutorial on spectral clustering. Stat. Comput. *17*, 395–416.

Wang, Q., and Burkhalter, A. (2007). Area map of mouse visual cortex. J. Comp. Neurol. *502*, 339–357.

Wang, Q., Ding, S.-L., Li, Y., Royall, J., Feng, D., Lesnar, P., Graddis, N., Naeemi, M., Facer, B., Ho, A., et al. (2020). The Allen Mouse Brain Common Coordinate Framework: A 3D Reference Atlas. Cell *181*, 936-953.e20.

Yamashita, T., and Petersen, C.C. (2016). Target-specific membrane potential dynamics of neocortical projection neurons during goal-directed behavior. ELife *5*.

Yang, H., Kwon, S.E., Severson, K.S., and O'Connor, D.H. (2016). Origins of choice-related activity in mouse somatosensory cortex. Nat. Neurosci. *19*, 127–134.

Zhao, S., Ting, J.T., Atallah, H.E., Qiu, L., Tan, J., Gloss, B., Augustine, G.J., Deisseroth, K., Luo, M., Graybiel, A.M., et al. (2011). Cell type–specific channelrhodopsin-2 transgenic mice for optogenetic dissection of neural circuitry function. Nat. Methods *8*, 745–752.

FIGURE LEGENDS

Figure 1. Learning of delayed whisker detection task changes licking patterns and orofacial movements

(A and B) Delayed whisker detection task. A, Behavioral setup. Sensory stimuli were delivered to head-restrained mice. Licking and orofacial movements were monitored using a piezoelectric lick sensor and a behavioral camera. B, Task structure. 200-ms visual and auditory cues were delivered in all trials separated by 2 seconds. In half of trials (Go trials), a 10-ms whisker stimulus was delivered 1 second after the visual cue onset, and mice were required to lick a spout for a reward after the auditory cue. In the other half of trials (No-Go trials), no whisker stimulus was delivered, and mice were required not to lick the spout. Licks before the auditory cue (early lick), and licks in trials without a whisker stimulus (False-alarm) were punished by a time out.

(C) Learning paradigm. All mice went through visual-auditory pretraining, where all licks after the auditory cue were rewarded. Expert mice went through whisker training where whisker stimulus was introduced in 50% of trials (Go), and only whisker trials were rewarded. Neural data were obtained in Novice and Expert mice, before and after whisker training respectively. The same mice were imaged during Novice and Expert stage, while different mice were used for electrophysiological recordings.

(D) Task performance. *Left*, Novice mice licked equally in Go and No-Go trials, whereas Expert mice licked preferentially in Go trials (quantified across all completed trials). Gray circles represent individual mice (Novice, n=15; Expert, n=25). *Right*, first lick time in all Go vs No-Go trials was similar in Novice mice, but differed in Expert mice. Expert mice made more early licks.

(E and F) Orofacial movements. E, Example Expert and Novice trials: extracted speed of left C2-whisker, jaw and tongue together with the lick sensor signal are plotted along the trial time-course. F, Average movement (mean ± SEM): Novice mice (n=8) moved the whisker, but did not move tongue and jaw before the auditory cue. Expert mice (n=18) reduced whisking before whisker stimulus, and increased tongue and jaw movements after the whisker stimulus. Asterisks represent statistical comparison of movement between Novice and Expert mice in: Baseline (0-800 ms), Whisker (1000-

1200 ms), Delay (1200-2000 ms) and Response (2000-3000 ms) windows (Wilcoxon rank-sum test, false discovery rate (FDR) corrected, ***: $p<0.001$, **: $p<0.01$, *: $p<0.05$). Only mice used for electrophysiology are plotted.

See also Figure S1.

Figure 2. Wide-field imaging reveals global changes in cortical processing

(A and B) Wide-field calcium imaging in Emx1-RCaMP mice. A, Fluorescence images of an ex-vivo fixed brain in dorsal view (*left*) and a coronal section of somatosensory area (*right*) showing RCaMP expression in pyramidal neurons in deep and superficial layers. B, In vivo fluorescence image of the tilted (24 degree) left dorsal hemisphere through transparent, intact skull preparation (*right*). In vivo images were registered to Allen Mouse Brain Atlas (*left*). Regions of interest during electrophysiological experiments are marked: wS1, primary somatosensory area for whisker; wS2, secondary somatosensory area for whisker; wM1, primary motor area for whisker; wM2, secondary motor area for whisker; Aud, auditory area; Vis, visual area; PPC, posterior parietal cortex; tjM1, primary motor area for tongue and jaw; tjM2/ALM, anterior lateral motor area.

(C-E) Time-course of global cortical activity in Hit trials for Novice vs Expert mice. C, functional images. Each frame shows instantaneous $\Delta F/F_0$ without averaging (10 ms/frame). For each pixel, baseline activity in a 50-ms window before visual cue onset was subtracted. Mean calcium activity of 62 Novice and 82 Expert sessions from 7 mice, Novice and Expert difference, and the statistical significance of the difference (*p*-value of Wilcoxon rank-sum test, FDR-corrected) are plotted from top to bottom. Green traces, anatomical borders based on Allen Mouse Brain Atlas. Black '+' indicates bregma. Note both activation and deactivation patterns during the delay period after whisker stimulus upon learning. D, calcium signal traces (mean ± SEM) in wS1 (top) and tjM1 (bottom) as depicted in B (ROI size, 7×7 pixels). Inset in tjM1, the traces after the whisker onset. Note a sharp decrease of the signal in tjM1. E, calcium signal (mean ± SEM) in early and late delay period (180-200 ms and 880-900 ms after whisker onset). Asterisks represent significant difference in calcium signal in each area comparing Novice and Expert mice (*, p<0.05, **, P<0.005, *** P<1x10-17; Wilcoxon rank-sum test, FDR-corrected).

See also Figure S2-3 and Videos S1-4.

Figure 3. Task epoch-specific processing across single neurons

(A) Map of silicon probe recordings of single units. Reconstructed location of silicon probes registered to Allen Mouse Brain Atlas in 2D dorsal view (*right*) in Expert (strong colors, filled circles) and Novice (light colors, open circles). Probes assigned to each anatomical region and their average coordinate (mean ± SEM) are shown with different colors. Medial prefrontal cortex, mPFC; dorsal hippocampal CA1, dCA1; dorsolateral striatum, DLS. Abbreviation of other regions are found in Figure 2B.

(B) Example neurons from expert mice. Raster plots and peristimulus time histograms (PSTHs) for three representative units in wS1, tjM2/ALM, and tjM1 encoding whisker, delay and licking, respectively. Four trial types are plotted separately.

(C) Time-lapse maps of mean firing rate in Novice and Expert mice in Hit trials. Circles represent different probes and colors show mean z-scored firing rate across the probe at each time window. Neuronal activity patterns are strikingly different between Novice and Expert mice during the delay period (1400 –1900 ms after visual cue onset).

(D) Population firing rate in Hit trials. Baseline-subtracted mean firing rate (mean ± SEM) in each region is superimposed for Expert (purple) and Novice (cyan) mice (*left*). Number of recorded neurons are shown alongside the firing rates for each area and mice group. *P*-value map of Expert vs Novice mice comparison in 50-ms non-overlapping windows (non-parametric permutation test, FDR-corrected) (*right*).

(E) Selectivity index in Novice and Expert mice. For individual neurons, selectivity between Hit versus Correct-rejection trials was determined in 100-ms non-overlapping windows based on area under the ROC curve. Percentage of significantly selective neurons in each region is shown across time in Novice (*left*) and Expert (*right*) mice. Significance of selectivity was determined using non-parametric permutation tests

(p<0.05). Note the increase in percentage of selective neurons in wM2 early after whisker stimulus and in tjM2/ALM throughout the delay period.

See also Figure S4 and Videos S5-6.

Figure 4. Acquired and stable firing patterns across learning

(A) Unsupervised neuronal clustering. Firing maps of all single units from Novice and Expert mice clustered based on their trial-type average normalized firing rate. Black horizontal lines separate different clusters. The color bar on the left shows weighted percentage of neurons in each cluster from Novice (cyan) and Expert (purple) mice.

(B) Within cluster distribution heatmaps. Proportion of neurons within each cluster belonging to different brain regions in Novice (*left*) and Expert (*right*) mice are shown. Proportions are normalized to the number of neurons recorded from each area to correct for different sample sizes.

(C) Spatial distribution of selected task-relevant clusters across brain regions. *Left*, weighted proportion of neurons belonging to different cortical regions (similar to rows of heatmaps in panel B) for whisker-responsive clusters (C2, C3, C4) and for delay-active clusters (C5-7, C17). *Right*, Density maps showing distribution of clusters across superficial (solid border) and deep (dotted border) brain regions for Novice (cyan border) and Expert (purple border) mice. Note that delay patterns (C5-6) appear after whisker training, but sharp sensory response patterns (C2, C3, C4) remain stable.

(D) Most prominent firing patterns in different brain regions. For each area (wS1, wM2, tjM2/ALM and tjM1), mean firing rate of neurons belonging to their two most representative clusters are shown for Expert and Novice mice. Note the preponderance of persistent-activity delay clusters in tjM2/ALM after whisker training. Numbers indicate cluster number and percentage of neurons from the area belonging to the cluster.

See also Figure S5.

Figure 5. Delay processing beyond preparatory movement

(A and B) Focalized delay activity in Quiet Hit trials. Imaging and neuronal data were averaged across selected Quiet trials with no preparatory jaw movements during the delay period (see STAR Methods). A, Wide-field calcium signal during the delay period in Quiet Hit trials (bottom). Each frame represents the mean signal during 50-ms period (280 to 320 ms) after whisker onset subtracted by the mean during a 50-ms period immediately before whisker onset. From top to bottom, mean calcium signal of 62 Novice and 82 Expert sessions from 7 mice, their difference, and the statistical significance of the difference (*p*-value of Wilcoxon rank-sum test, FDR-corrected). Note that in Quiet trials, delay activity gets restricted to tjM2/ALM, while deactivation in orofacial sensorimotor regions becomes broader and stronger. B, Mean firing rate in Expert and Novice mice in Quiet Hit trials (*left*) and *p*-value map of Expert/Novice comparison in 50-ms non-overlapping windows (non-parametric permutation test, FDR-corrected) (*right*). Only tjM2/ALM neurons in Expert mice showed a sustained firing throughout the delay period in Quiet trials.

(C-E) Poisson encoding model capturing trial-by-trial neuronal variability. C, *left*, fraction of neurons significantly encoding Whisker (*top*), Delay (*middle*) and Prelick (*bottom*) (p<0.05, likelihood ratio test, See STAR Methods) in different regions. Asterisks represent significant change comparing fraction of Novice and Expert neurons (proportion test, ***: p<0.001, **: p<0.01, *: p<0.05). *Right*, for each of the Whisker, Delay and Prelick model variables, average model weight maps across neurons of superficial (solid border) and deep (dotted border) brain regions of Expert and Novice are shown. D, Venn diagrams showing the amount of overlap among neuronal populations in different regions significantly encoding Whisker, Delay and Prelick variables. The size of the circles are proportional to the fraction of significantly modulated neurons. E, Comparison of reconstructed PSTHs of Quiet trials (dotted lines) with empirical data (solid lines). Note that the model fitted to all trials (black) also reconstructs well Quiet (blue) trials.

See also Figure S6 and Table S1.

Figure 6. Conversion of a sensory signal into a motor plan

(A) Wide-field signal after whisker stimulus in Novice and Expert mice in Hit trials. Each frame shows the instantaneous calcium activity (10 ms/frame). Mean signal during 50-ms period immediately before whisker onset is subtracted. From top to bottom, average calcium signal of 62 Novice and 82 Expert sessions from 7 mice, their difference, and the statistical significance of the difference (p-value of Wilcoxon rank-sum test, FDR-corrected).

(B) Sequential propagation of whisker-evoked neuronal response in Hit trials (*left*, Novice; *right*, Expert). Mean *z*-scored firing rate in the first 100-ms window after whisker stimulus are shown. Brain regions are sorted based on their onset latency in Expert mice.

(C) Latency of whisker-evoked response. Cumulative distribution of single neuron latencies for key cortical areas in Novice (*left*) and Expert (*middle*) mice. Distribution of latencies across different areas and their change across learning (*right*). Note increased latency of wM1 neurons in Expert mice, whereas the latency of wM2 neurons decreased in Expert mice.

(D) Early whisker-evoked spiking activity in Hit trials. Baseline-subtracted (50-ms prior to whisker onset) mean firing rate across critical cortical areas in Expert and Novice mice are overlaid. Gray horizontal bars represent the *p*-value of Novice/Expert comparison in 50-ms consecutive windows (non-parametric permutation test, FDR-corrected). Note the earliest increase in whisker-evoked response upon learning in wM2.

(E) Spiking activity in Hit vs Miss trials. Baseline-subtracted (50-ms prior to whisker onset) mean firing rate across critical cortical areas in Hit and Miss trials of Expert mice are overlaid. Gray horizontal bars represent the *p*-value of Hit/Miss comparison in 50-ms consecutive windows (non-parametric permutation test, FDR-corrected). Note the earliest significant difference in wM2.

See also Figure S7.

Figure 7. Spatiotemporally specific causal involvement of cortical regions

(A) Spatiotemporally specific optogenetic inhibition in VGAT-ChR2 transgenic mice. Blue shaded areas represent inhibition windows across trial-timeline (*top*).

(B) Behavioral impact of optogenetic inactivation across time windows for each brain region (mean ± SEM) . For each area, Hit rate (black) and False-alarm rate (red) are plotted for Light-off (Off), Baseline (B), Whisker (W), Delay (D) and Response (R) windows. Asterisks represent significant difference comparing Hit (black) and False-alarm (red) in light trials vs light-off control trials (n=9 mice; *, $p<0.05$, **, $P<0.01$, *** $P<0.001$; Wilcoxon signed-rank test, Bonferroni correction for multiple comparison).

(C) Spatiotemporal map of behavioral impact of focal inhibition in Go (*middle*) and No-Go trials (*bottom*). Circles represent different cortical regions labeled on the schematic (*bottom right*); color shows change in Lick probability and circle size shows the *p*-value of the significance test comparing light trials vs light-off control trials (n=9 mice, Wilcoxon signed-rank test, Bonferroni correction for multiple comparison).

Figure 8. Spatiotemporally specific causal involvement of cortical regions

(A) A causal involvement index was defined as the region- and epoch-specific difference in firing rate comparing Hit and Correct-rejection trials (n=25, Expert mice) multiplied by the change in hit rate induced by optogenetic inactivation (n=9, VGAT-ChR2 mice). Error bars are obtained from bootstrap (see STAR Methods) and represent standard deviation (bootstrap standard error). Asterisks represent significance level (*, $p<0.05$, **, $P<0.01$, *** $P<0.001$; non-parametric permutation test, Bonferroni correction for multiple comparison).

(B) Proposed cortical circuits connecting whisker somatosensory cortex to tongue/jaw anterolateral secondary motor cortex upon task learning.

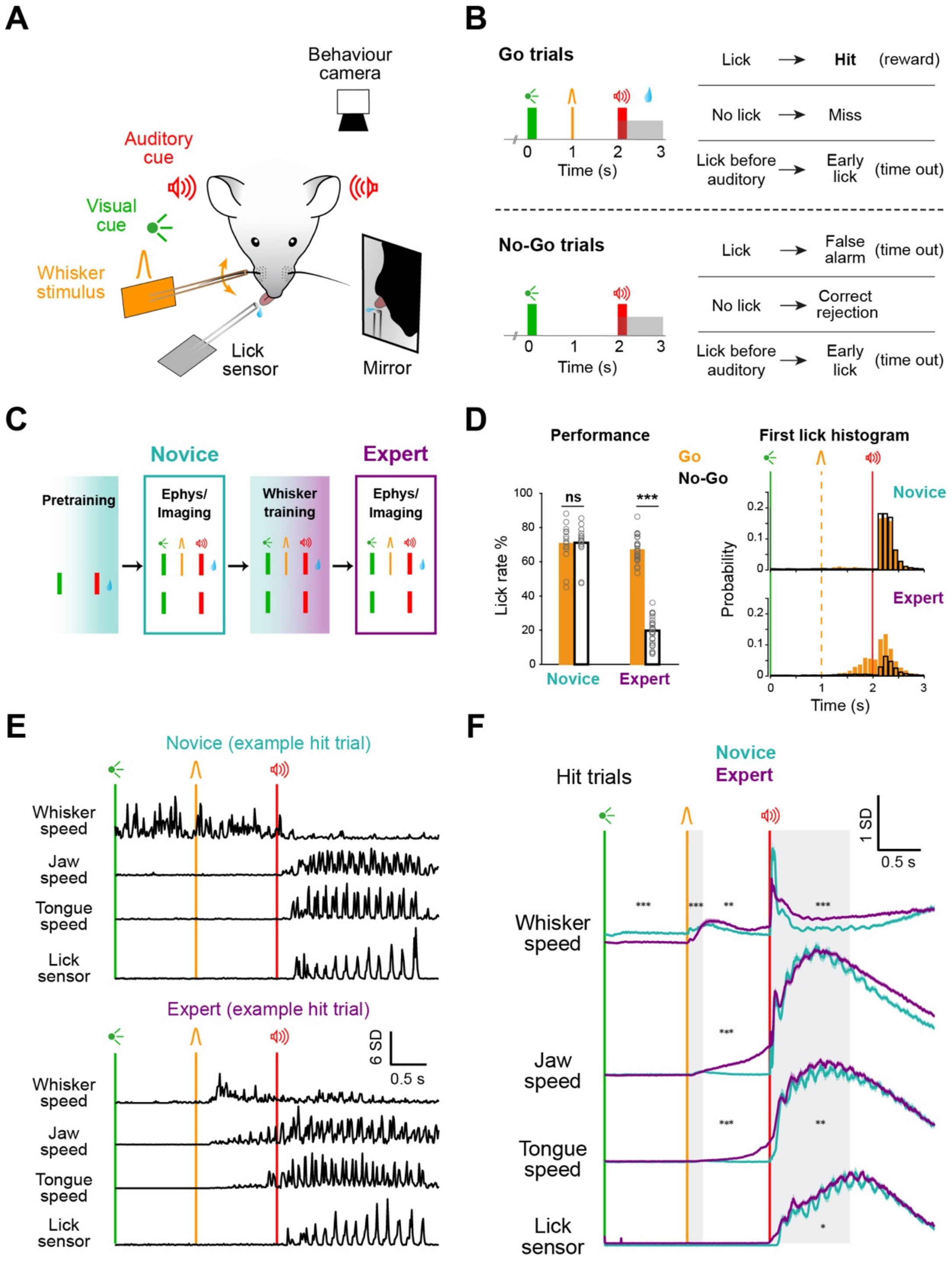

Figure 1
Esmaeili et al.

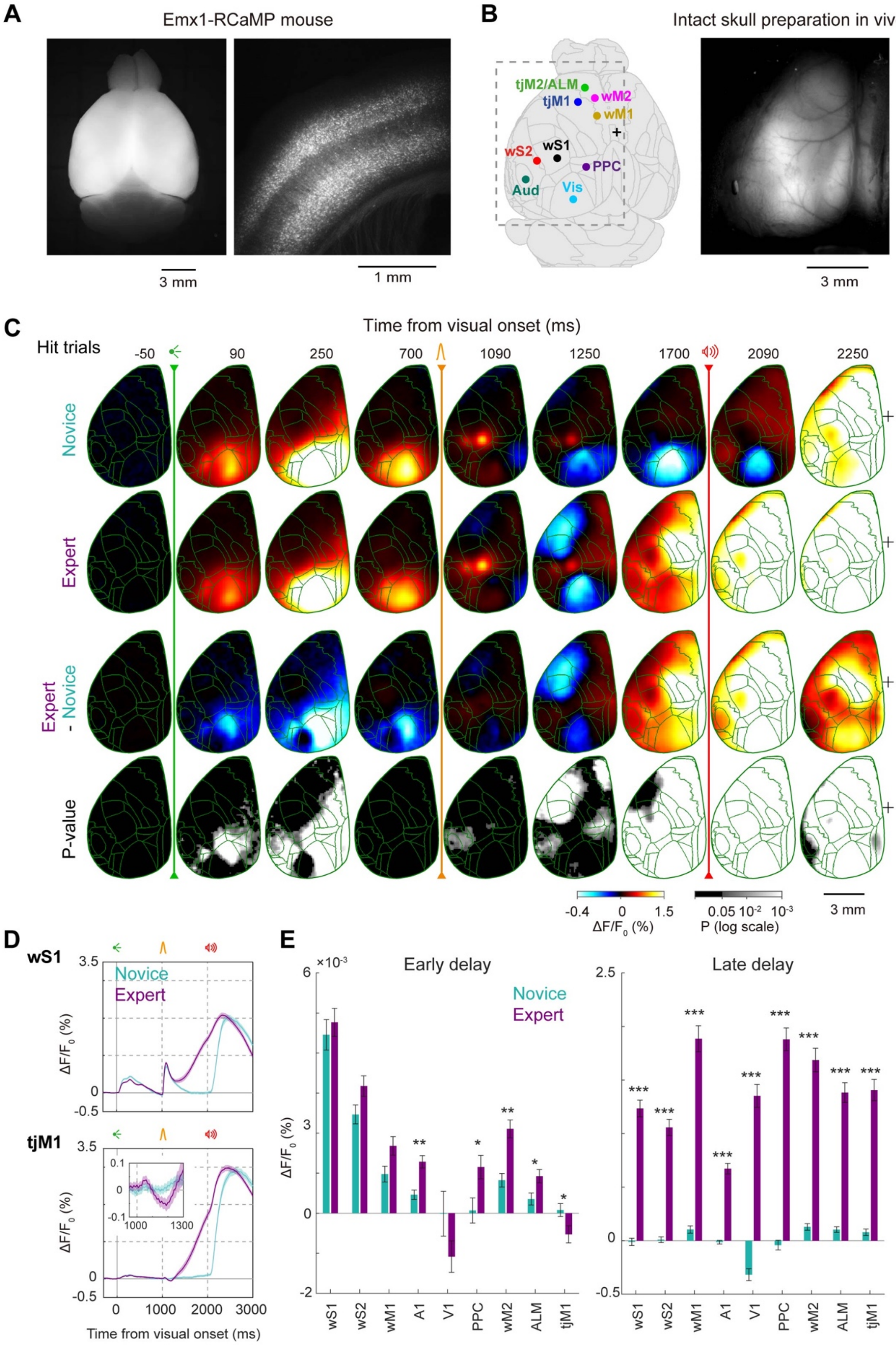

Figure 2
Esmaeili et al.

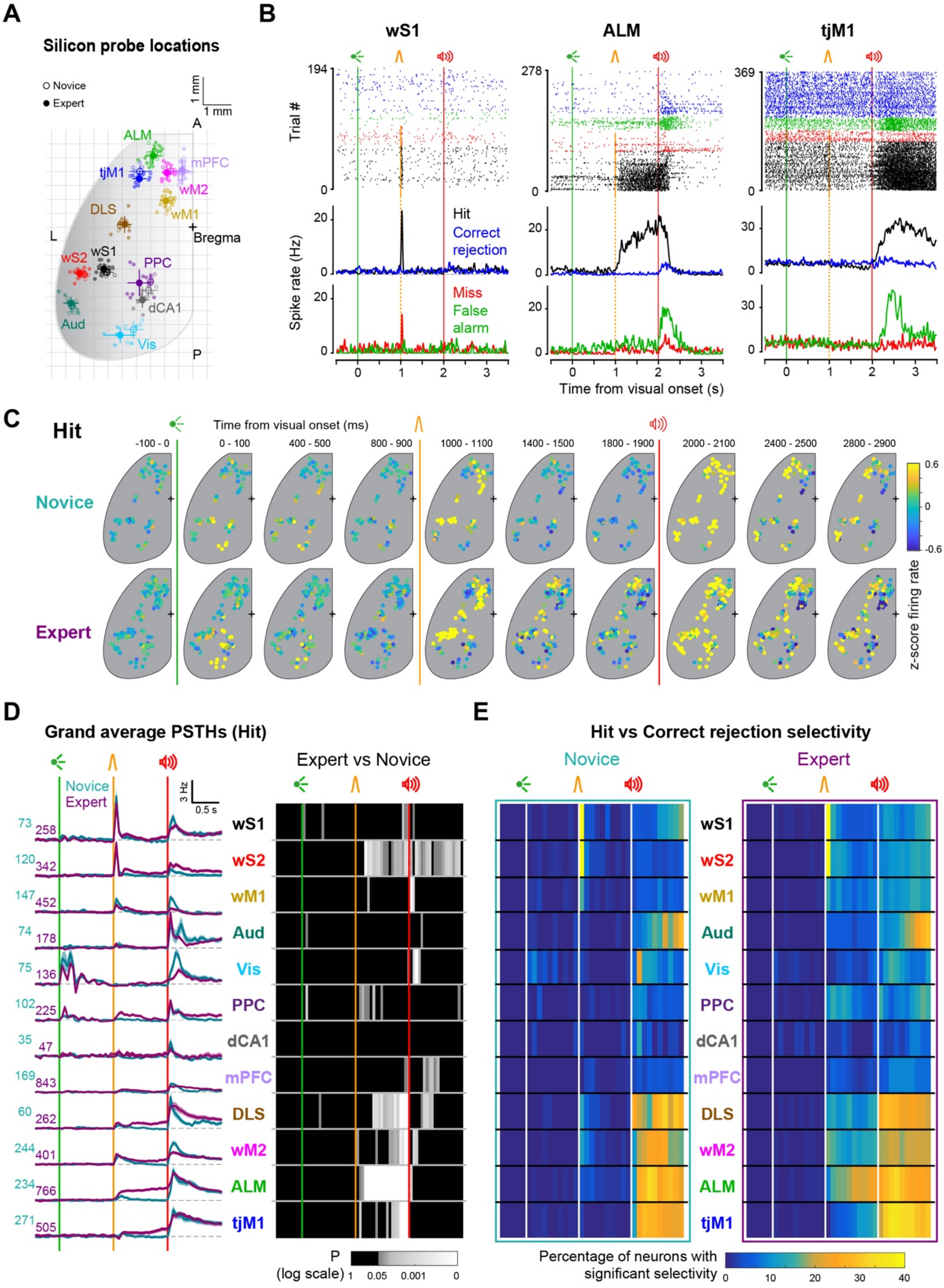

Figure 3
Esmaeili et al.

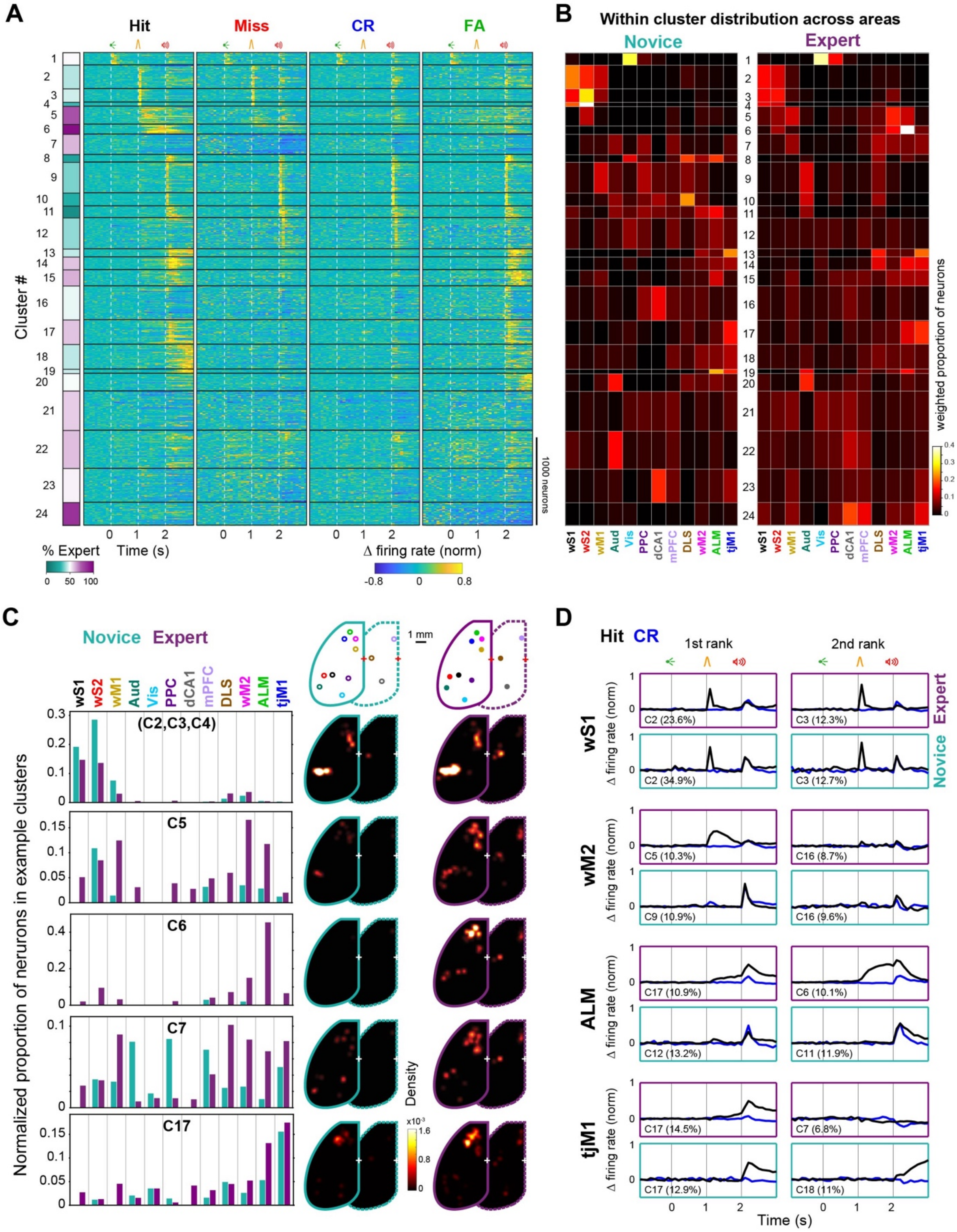

Figure 4
Esmaeili et al.

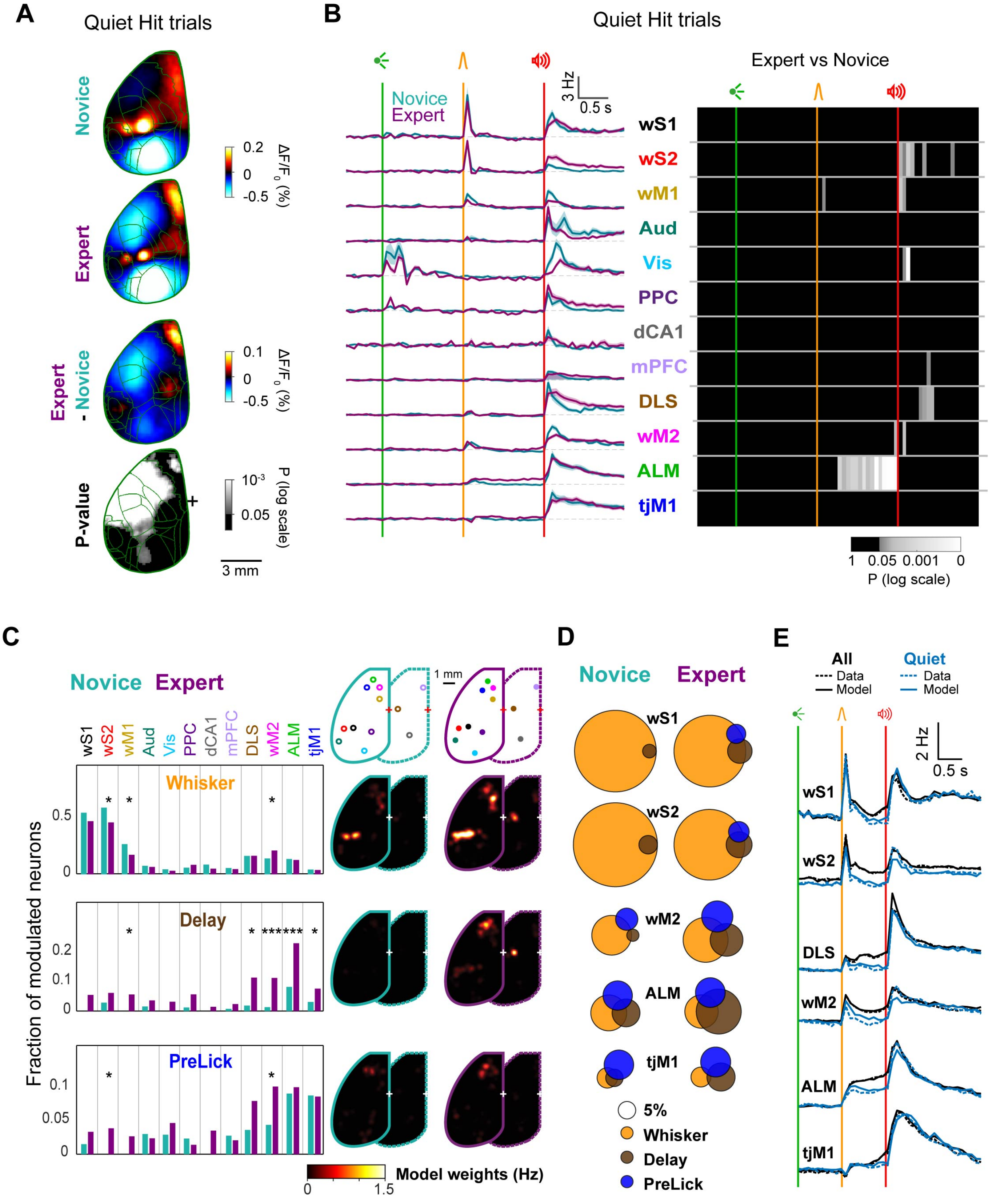

Figure 5
Esmaeili et al.

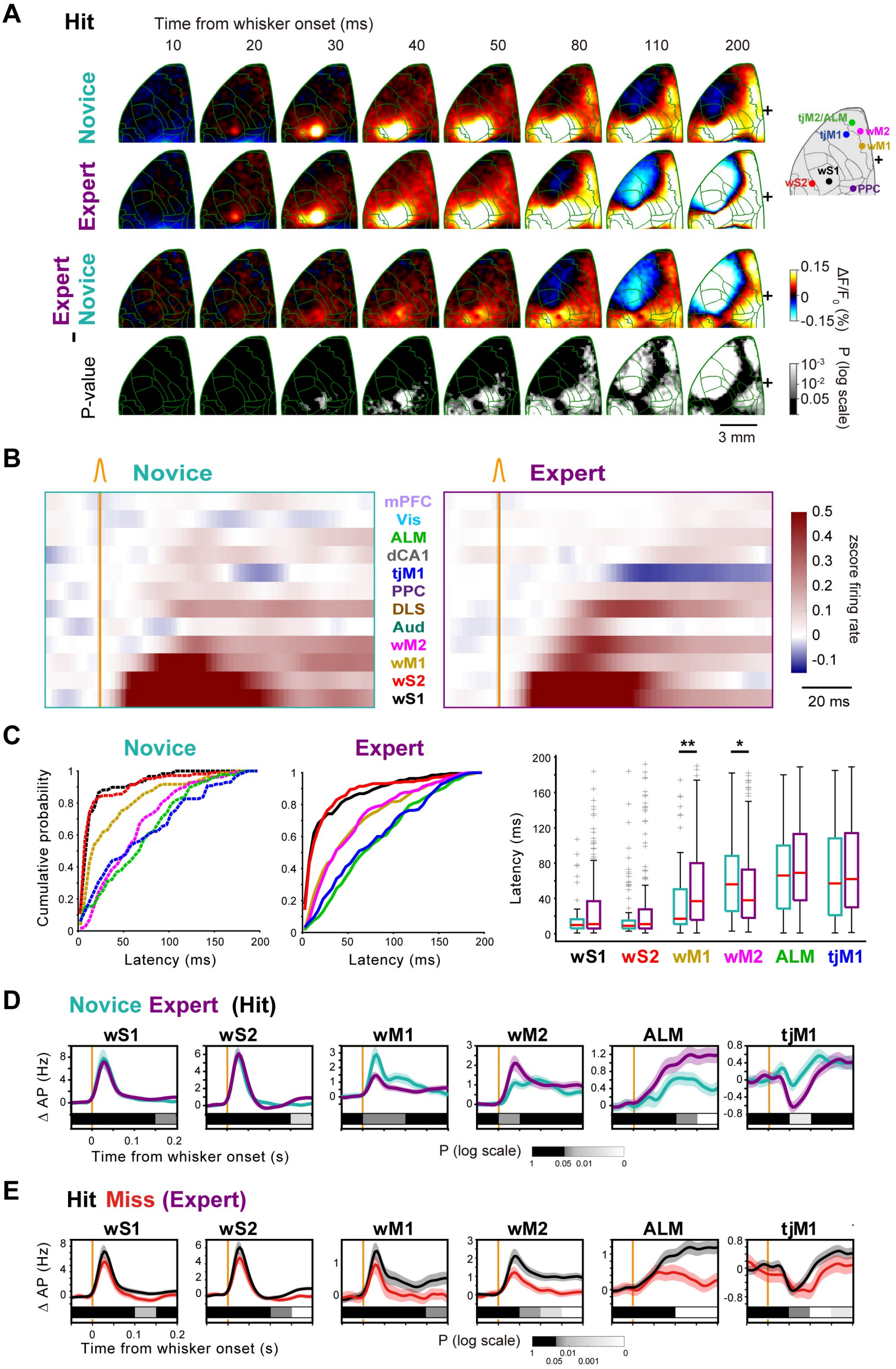

Figure 6
Esmaeili et al.

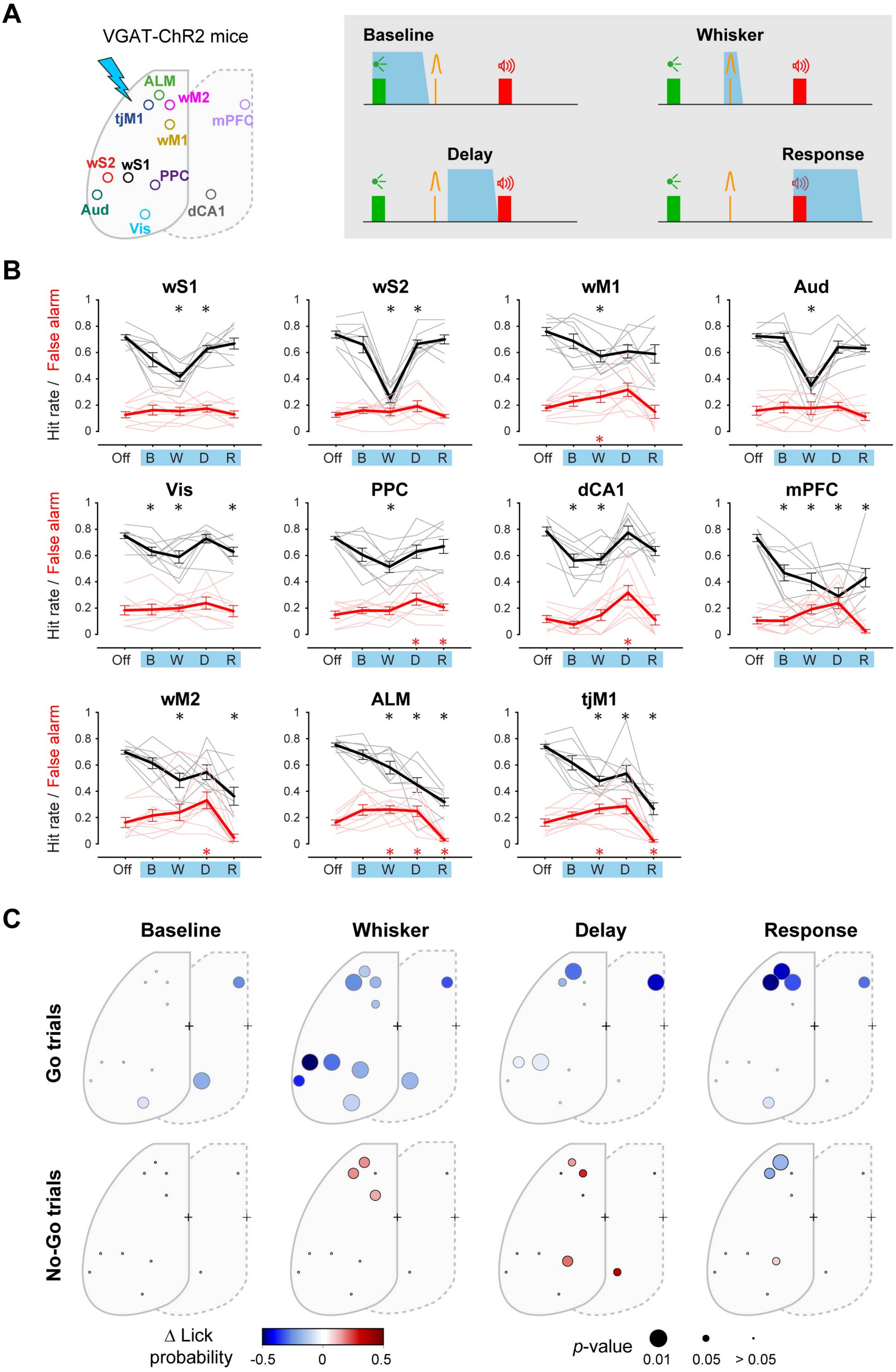

Figure 7
Esmaeili et al.

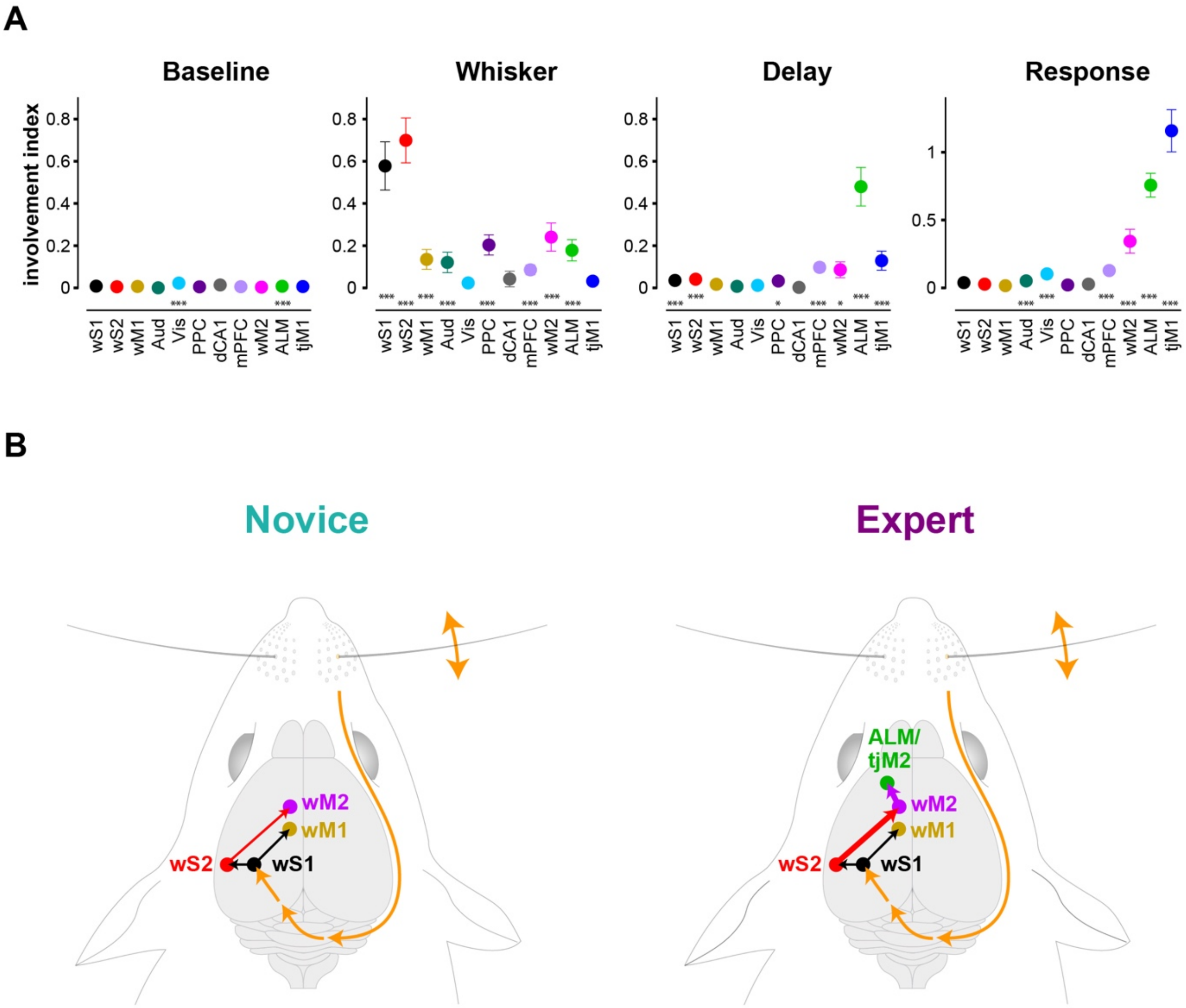

Figure 8
Esmaeili et al.

MATERIALS AND METHODS

KEY RESOURCES TABLE

REAGENT or RESOURCE	SOURCE	IDENTIFIER
Chemicals, Peptides, and Recombinant Proteins		
DiI (1,1'-Dioctadecyl-3,3,3',3'-Tetramethylindocarbocyanine Perchlorate)	Invitrogen, USA	Cat# D282
Loctite super glue	Henkel, Germany	401
Silicon elastomer	World Precision Instruments, USA	Kwik-Cast
32% paraformaldehyde (PFA)	Electron Microscopy Science, USA	32% PFA solution
Oxidized agarose	Merck KGaA, Germany	Type-I agarose
Sodium borohydride	Merck KGaA, Germany	NaBH4,
Self-curing denture acrylic	Kulzer, Germany	Paladur
Self-curing denture acrylic (transparent)	LANG, USA	Ortho-Jet
Deposited Data		
Data set and MATLAB analysis code	This study	https://zenodo.org/communities/petersen-lab-data
Allen Mouse Common Coordinate Framework version 3	Wang et al., 2020	http://help.brain-map.org/display/mousebrain/API
Experimental Models: Organisms/Strains		
Mouse: B6.129S2-Emx1<tm1(cre)Krj>/J	The Jackson Laboratory	JAX: 005628
Mouse: B6.Cg-Tg(Camk2a-tTA)1Mmay/DboJ	The Jackson Laboratory	JAX: 007004
Mouse: B6.Cg-Igs7<tm143.1(tetO-RcaMP1.07)Hze>/J	The Jackson Laboratory	JAX: 030217
Mouse: STOCK Vip<tm1(cre)Zjh>/J	The Jackson Laboratory	JAX: 010908

Mouse: B6.Cg-Gt(ROSA)26Sor<tm9(CAG-tdTomato)Hze>/J	The Jackson Laboratory	JAX: 007909
Mouse: B6.Cg-Tg(Slc32a1-COP4*H134R/EYFP)8Gfng/J	The Jackson Laboratory	JAX: 014548
Mouse: C57BL/6 wild type	The Jackson Laboratory	
Mouse: B6.FVB(Cg)-Tg(Adora2a-cre)KG139Gsat/Mmucd	Mutant Mouse Resource & Research Centers	MMRRC: 036158
Software and Algorithms		
Matlab R2020a	MathWorks, USA	SCR_001622
Klusta	Rossant et al., 2016	https://github.com/kwikteam/klusta
Two-photon microscopy control software	Vidrio Technologies, USA	ScanImage 2017b
Extension for serial sectioning in 2-P tomography	Han et al., 2018	BakingTray https://github.com/BaselLaserMouse/BakingTray
ARAtools	Han et al., 2018	https://github.com/SainsburyWellcomeCentre/ara_tools
StitchIt	Han et al., 2018	https://github.com/BaselLaserMouse/StitchIt
MaSIV	Han et al., 2018	https://github.com/alexanderbrown/masiv
Other		
32-channel silicon probe	NeuroNexus,USA	A1x32-Poly2-10mm-50s-177
Optrode	NeuroNexus, USA	A1x32-Poly3-10mm-50s-177-OA32,
Digital headstage	Blackrock Microsystems, USA	CerePlex™ M32
Data acquisition system	Blackrock Microsystems, USA	CerePlex™ Direct
470-nm high power LED	Thorlabs, USA	M470F3
Blue Laser	GMP SA, Switzerland	MBL-F-473/200mW

High speed camera	Optronis, Germany	CL 600 X 2/M
16-bit monochromatic sCMOS camera	Hamamatsu Photonics, Japan	ORCA FLASH4.0v3,
567-nm LED	Luxeon, Canada	SP-01-L1
563/9-nm band pass filter	Semrock, USA	563/9 BrightLine HC
645/110 band pass filter	Semrock, USA	645/110 ET Bandpass
588-nm dichroic mirror	Chroma, USA	Beamsplitter T 588 LPXR
Nikkor 50 mm f/1.2 lens	Nikon, Japan	50 mm f/1.2
50 mm video lens	Navitar, USA	50 mm f/1.4
High-precision X/Y/Z stage	Physik Instrumente, Germany	X/Y: V-580 Z: L-310
High-precision piezo objective scanner	Physik Instrumente, Germany	PIFOC P-725
500 – 550 nm bandpass filter	Chroma, USA	ET525/50
580 – 630 nm bandpass filter	Chroma, USA	ET605/70
A 16x water immersion objective lens	Nikon, Japan	LWD 16x/0.80W; MRP07220
Vibratome for 2-P tomography	Leica, Germany	VT1000S
Vibratome for conventional histology	Leica, Germany	VT 100

LEAD CONTACT AND MATERIALS AVAILABILITY

Further information and requests for resources and reagents should be directed to and will be fulfilled by the Lead Contact, Carl Petersen (carl.petersen@epfl.ch). This study did not generate new unique reagents.

EXPERIMENTAL MODEL AND SUBJECT DETAILS

All procedures were approved by Swiss Federal Veterinary Office (License number VD-1628) and were conducted in accordance with the Swiss guidelines for the use of research animals. For calcium imaging, we produced RCaMP mice by crossing Emx1-

IRES-Cre mice [B6.129S2-Emx1<tm1(cre)Krj>/J, JAX: 005628] (Gorski et al., 2002), CamK2a-tTA mice [B6.Cg-Tg(Camk2a-tTA)1Mmay/DboJ, JAX: 007004] (Mayford et al., 1996), and TITL-R-CaMP mice [TIGRE1.0-RCaMP, B6.Cg-Igs7<tm143.1(tetO-RcaMP1.07)Hze>/J, JAX: 030217, kind gift from Fritjof Helmchen (University of Zurich)] (Bethge et al., 2017). For control imaging, we produced tdTomato mice by crossing VIP-IRES-Cre mice [STOCK Vip<tm1(cre)Zjh>/J, JAX: 010908] (Taniguchi et al., 2011) and LSL-tdTomato mice [B6.Cg-Gt(ROSA)26Sor<tm9(CAG-tdTomato)Hze>/J, JAX: 007909] (Madisen et al., 2010). For optogenetic inactivation, we used VGAT-ChR2-EYFP mice [B6.Cg-Tg(Slc32a1-COP4*H134R/EYFP)8Gfng/J, JAX: 014548] (Zhao et al., 2011). For electrophysiological recording, we used C57BL/6 wild type mice, and VGAT-ChR2-EYFP mice, as well as Adora2aCre mice [B6.FVB(Cg)-Tg(Adora2a-cre)KG139Gsat/Mmucd, MMRRC: 036158] (Gong et al., 2007) crossed with LSL-tdTomato mice. Adult male and female mice were at least 6-weeks-old at the time of head-post implantation (see below). Mice were kept in a reverse light/dark cycle (light 7 p.m. to 7 a.m.), in ventilated cages at a temperature of 22 ± 2°C with food available ad libitum. Water was restricted to 1 ml a day during behavioral training with at least 2 days of free-access to water in the cage every 2 weeks. All mice were weighed and inspected daily during behavioral training.

METHOD DETAILS

Experimental design

This study did not involve randomization or blinding. We did not estimate sample-size before carrying out the study. However, the sample-size in this study is comparable with those used in related studies (Allen et al., 2017; Guo et al., 2014; Harvey et al., 2012; Hattori et al., 2019; MacDowell and Buschman, 2020; Pinto et al., 2019).

Implantation of metal headpost

Mice were deeply anesthetized with isoflurane (3% with O_2) and then were maintained under anesthesia using a mixture of ketamine and xylazine injected intraperitoneally (ketamine: 125 mg/kg, xylazine: 10 mg/kg). Carprofen was injected intraperitoneally (100 μl at 0.5 mg/ml) for analgesia before the start of surgery. Body temperature was kept at 37°C throughout the surgery with a heating pad. An ocular ointment (VITA-POS, Pharma Medica AG, Switzerland) was applied over the eyes to prevent them from drying. As local analgesic, a mix of lidocaine and bupivacaine was injected below the scalp before any surgical intervention. A povidone-iodine solution (Betadine, Mundipharma Medical Company, Bermuda) was used for skin disinfection. To expose the skull, a part of the scalp was removed with surgical scissors. The periosteal tissue was removed with cotton buds and a scalpel blade. After disinfection with Betadine and rinsing with Ringer solution, the skull was dried well with cotton buds. A thin layer of super glue (Loctite super glue 401, Henkel, Germany) was then applied across dorsal part of the skull and a custom-made head fixation implant was glued to the right hemisphere without a tilt and parallel to the midline. A second thin layer of the glue was applied homogeneously on the left hemisphere. After the glue was dried, the head implant was further secured with self-curing denture acrylic (Paladur, Kulzer, Germany; Ortho-Jet, LANG, USA). For electrophysiological recordings a chamber was made by building a wall with denture acrylic along the edge of the bone covering the left hemisphere. Particular care was taken to ensure that the left hemisphere of the dorsal cortex was free of denture acrylic and only covered by super glue for optical access. This intact, transparent skull preparation was used to perform wide-field calcium imaging as well as intrinsic optical signal (IOS) imaging experiments. The animal was returned to its home cage and ibuprofen (Algifor Dolo Junior, VERFORA SA, Switzerland) was given in the drinking water for three days after surgery.

Skull preparation and craniotomies

For wide-field calcium imaging, an intact transparent skull was used as described above. For electrophysiological recordings, up to 10 small craniotomies were made over the regions of interest using a dental drill under isoflurane anesthesia (2-3% in O_2). The craniotomies were protected using a silicon elastomer (Kwik-Cast, World Precision Instruments, Sarasota, FL, USA). Regions of interest were selected based on the hotspots of activity from wide-field calcium imaging experiments, functionally relevant areas based on our previous studies (Esmaeili and Diamond, 2019; Guo et al., 2014; Harvey et al., 2012; Le Merre et al., 2018; Mayrhofer et al., 2019; Sachidhanandam et al., 2013; Sippy et al., 2015; Sreenivasan et al., 2016) and intrinsic optical signal (IOS) imaging (Sachidhanandam et al., 2013). IOS was performed under isoflurane anesthesia (1-1.5% with O_2) to map the C2-whisker representation in primary and secondary whisker somatosensory cortex (wS1 and wS2), as well as the auditory area (Aud). A piezoelectric actuator was used to vibrate the right C2 whisker, or to generate rattle sounds. Increase in absorption of red light (625 nm) upon sensory stimulation indicated the functional location of the corresponding sensory cortex. For the other regions stereotaxic coordinates relative to bregma were used: primary and secondary whisker motor cortices (wM1: AP 1.0 mm; Lat 1.0 mm and wM2: AP 2.0 mm; Lat 1.0 mm), primary and secondary tongue/jaw motor cortices (tjM1: AP 2.0 mm; Lat 2.0 mm and tjM2/ALM: AP 2.5 mm; Lat 1.5 mm), visual cortex (Vis: AP -3.8 mm; Lat 2.5 mm), posterior parietal cortex (PPC: AP -2 mm; Lat 1.75 mm), medial prefrontal cortex (mPFC: AP 2 mm; Lat 0.5 mm), dorsal part of the CA1 region of the hippocampus (dCA1: AP -2.7 mm; Lat 2.0 mm) and dorsolateral striatum (DLS: AP 0.0 mm; Lat 3.5 mm). For optogenetic inactivation experiments the bone over the regions of interest was thinned and a thin layer of superglue was applied to protect the skull for stable optical access over days. For the inactivation of mPFC and dCA1 a small craniotomy was made for the insertion of an optical fiber or an optrode.

Behavioral paradigm

A total of 49 mice were examined in the delayed whisker detection task including 9 RCaMP, 24 wild-type or negative, 9 VGAT-ChR2 and 7 tdTomato mice. During the behavioral experiments, all whiskers were trimmed except for the C2 whiskers on both sides, and the mice were water restricted to 1 ml of water/day. Mice were trained daily with one session/day and their weight and general health status were carefully monitored using a score sheet. Both groups of mice (Expert and Novice) went through a 'pre-training' phase which consisted of trials with visual and auditory cues (without any whisker stimulus) (Figure 1C). Mice were rewarded by licking a spout, placed on their right side, in a 1-second response window after the auditory cue onset. Trials were separated 6-8 seconds and started after a quiet period of 2-3 seconds in which mice did not lick the spout. Each trial consisted of a visual cue (200-ms green LED) and an auditory cue (200-ms 10-KHz tone of 9 dB added on top of the continuous background white noise of 80 dB). The stimuli were separated with a delay period which gradually was increased to 2 seconds. Licking before the response period (i.e. ‘early lick’) aborted the trial and introduced a 3-5 second timeout. After 3-6 days of pre-training, mice learned to lick the spout by detecting the auditory cue and suppressed the early licks.

The wide-field imaging and electrophysiological recordings from the ‘Novice’ group of mice was performed when mice finished the pre-training phase and were introduced to the whisker delay task (Figure 1C). In this phase a whisker stimulus (10-ms Gaussian pulse through a glass tube attached to a piezoelectric driver) was delivered to the right C2 whisker 1 second after the visual cue onset in half of the trials. Importantly, the reward was available only in trials with the whisker stimulus referred to as ‘Go’, and time-out punishment (together with an auditory buzz tone) was given when mice licked in trials without the whisker stimulus referred to as ‘No-Go’ (Figure 1B). Thus, mice were requested to use the whisker stimulus to change their lick/no-lick behavior. Since the whisker stimulus was very weak, Novice mice continued licking in most of Go and No-Go trials irrespective of the whisker stimulus and did not show any sign of learning (Figure 1D and S1B).

The Expert mice entered a ‘whisker-training’ phase of 2-29 days during which a stronger whisker stimulus (larger amplitude and/or train of pulses) was introduced (Figure S1A). As the mice learned to lick correctly, the whisker stimulus amplitude was gradually returned to a smaller amplitude, eventually matching that delivered to Novice mice. Expert mice decreased licking in No-Go trials but increased their premature early licks after the whisker stimulus as monitored by the piezoelectric lick sensor and behavioral filming (Figure 1D and Figure S1B, see below). Behavioral hardware control and data collection were carried out using data acquisition boards (National Instruments, USA) and custom-written Matlab codes (MathWorks).

Quantification of orofacial movements

Contacts of the tongue with the reward spout were detected by a piezo-electric sensor. Continuous movements of the left C2 whisker, tongue and jaw were filmed by a high-speed camera (CL 600 X 2/M, Optronis, Germany; 200 or 500 Hz frame rate, 0.5- or 1-ms exposure, and 512x512-pixel resolution) under blue light or infrared illumination.

Movements of each body part were tracked using custom-written Matlab codes. For the imaging sessions, arc regions-of-interest were defined around the basal points for both the whisker and jaw (Mayrhofer et al., 2019). Crossing points on these arcs were detected for the whisker (the pixels with the minimum intensity) and the jaw (pixels with the maximum slope of intensity). A vector was then defined for each pair of basal point and the cross point, and the absolute angle was calculated for each vector with respect to midline. For the electrophysiology sessions, whisker angular position was quantified in a similar manner while movements of tongue and jaw were quantified as the changes in mean image intensity within a rectangular regions-of-interest (ROI) defined separately on the tracks of tongue and jaw. These signals were then normalized to the area covered by tongue and jaw ROIs. Absolute derivative of orofacial time series (whisker/jaw/tongue speed), were used for analysis of wide-field imaging and electrophysiology data.

Wide-field calcium imaging

Mice were mounted with a 24-degree tilt along the rostro-caudal axis. The red fluorescent calcium indicator R-CaMP1.07 or the red fluorescent protein tdTomato were excited with 563-nm light (567-nm LED, SP-01-L1 , Luxeon, Canada; 563/9-nm band pass filter, 563/9 BrightLine HC, Semrock, USA) and red emission light was detected through a band pass filter (645/110 ET Bandpass, Semrock). A dichroic mirror (Beamsplitter T 588 LPXR, Chroma, USA) was used to separate excitation and emission light. Through a face-to-face tandem objective (Nikkor 50 mm f/1.2, Nikon, Japan; 50 mm video lens, Navitar, USA) connected to a 16-bit monochromatic sCMOS camera (ORCA FLASH4.0v3, Hamamatsu Photonics, Japan), images of the left dorsal hemisphere were acquired with a resolution of 256x320-pixels (4x4 binning) aligned in rostro-caudal axis at a frame rate of 100 Hz (10-ms exposure). Behavioral task and imaging were synchronized by triggering acquisition of each image frame by digital pulses sent by the computer for behavioral task control. For each trial, 600 frames (6 seconds) of images were acquired from 1 second before the visual cue onset to 3 seconds after the auditory cue onset. To control for calcium-independent changes in cortical fluorescence, we also imaged transgenic mice expressing a red fluorescence protein tdTomato under vasoactive intestinal peptide promoter (tdTomato mice), which had a similar level of cortical fluorescence to RCaMP mice.

Electrophysiological recording

Extracellular spikes were recorded using single-shank silicon probes (A1x32-Poly2-10mm-50 s-177, NeuroNexus, MI, USA) with 32 recording sites covering 775 µm of the cortical depth. In each session two probes were inserted in two different brain targets acutely. Probes were coated with DiI (1,1'-Dioctadecyl-3,3,3',3'-Tetramethylindocarbocyanine Perchlorate, Invitrogen, USA) for post-hoc recovery of the recording location (see below). The neural data were filtered between 0.3 Hz and 7.5 kHz and amplified using a digital headstage (CerePlex™ M32, Blackrock Microsystems, UT, USA). The headstage digitized the data with a sampling frequency of 30 kHz. The digitized signal was transferred to our data acquisition system (CerePlex™ Direct, Blackrock Microsystems, UT, USA) and stored on an internal HDD of the host PC for offline analysis.

Optogenetic inactivation

Optogenetic inactivations were performed in 9 VGAT-ChR2 mice trained in the delay whisker task (similar to the Expert mice). An ambient blue masking light was used in the training sessions as well as testing days. Testing sessions started when mice reached Expert levels of performance (d-prime>1). All the areas of interest were examined in each mouse by inactivating one area per session. The order for the areas was randomized across mice, but inactivations of deep areas (mPFC and dCA1) were performed last. Three sessions per superficial area were performed in each mouse, followed by one session for each deep area. An optic fiber (400 µm; NA = 0.39, Thorlabs) coupled to a 470 nm high power LED (M470F3, Thorlabs, USA) was positioned in contact to the thinned bone for superficial areas or inserted above the left dCA1 at a depth of 1000 µm below the pia. In a subset of mice, dCA1 inactivation was performed using an optrode (silicon probe with an attached optical fiber: 100 µm; NA = 0.22, A1x32-Poly3-10mm-50 s-177-OA32, NeuroNexus, MI, USA). A similar optrode was used for all mPFC inactivations by inserting the tip of the fiber at a depth of 1700 µm, just above the prelimbic area of mPFC. The optrodes were connected to a blue Laser (MBL-F-473/200mW, GMP SA, Switzerland).

Light trials were randomly interleaved with light-off control trials and made up 1/3 of Go and No-Go trials. On light trials, a 100 Hz (40 Hz with laser) train of blue light pulses (50-65% duty cycle, mean power 8-10 mW) was applied in one of the 4 possible windows: ‘baseline’ (from visual cue onset to 800 ms after), ‘whisker’ (from 100 ms before the whisker onset to 100 ms after), ‘delay’ (from 200 ms after the whisker onset to 900 ms after) and ‘response’ (from auditory cue onset to 1000 ms after). All light windows were terminated by a 100 ms ramping down to prevent rebound excitation. In total, 21,293 light trials were tested in 9 mice, 11 areas and 4 trial epochs. On average, for each area and trial epoch, 60.7 ± 6.6 (mean ± SD) light trials were delivered for superficial areas in each mouse across 3 sessions; for deep areas (i.e. mPFC and dCA1), 22.4 ± 4 light trials were examined in one session.

Histology and localization of electrode/optical fiber tracks

At the end of experiments mice were perfused with phosphate buffered saline (PBS) followed by 4% paraformaldehyde (PFA, Electron Microscopy Science, USA) in PBS. The brain was post-fixed overnight at room temperature. Expression of RCaMP was observed by epifluorescence microscope in serial 100-µm coronal sections cut by a conventional vibratome (VT 1000S; Leica, Wetzlar, Germany). The DiI track of silicon probes were identified with either two-photon tomography (Mayrhofer et al., 2019) or conventional histological analysis. For three-dimensional imaging with two photon tomography, we embedded the brains in 3-5 % oxidized agarose (Type-I agarose, Merck KGaA, Germany) and covalently cross-linked the brain to the agarose by incubating overnight at 4 °C in 0.5 – 1 % sodium borohydride ($NaBH_4$, Merck KGaA, Germany) in 0.05 M sodium borate buffer. We imaged the brains in a custom-made two-photon serial microscope, which was controlled using Matlab-based software (ScanImage 2017b, Vidrio Technologies, USA) and BakingTray https://github.com/BaselLaserMouse/BakingTray, version master: 2019/05/20, extension for serial sectioning) (Han et al., 2018). The setup consists of a two-photon microscope coupled with a vibratome (VT1000S, Leica, Germany) and a high-precision X/Y/Z stage (X/Y: V-580; Z: L-310, Physik Instrumente, Germany). The thickness of a physical slice was set to be 50 µm for the entire brain and we acquired optical sections at 25 µm using a high-precision piezo objective scanner (PIFOC P-725, Physik Instrumente, Germany) in two channels (green channel: 500 – 550 nm, ET525/50, Chroma, USA; red channel: 580 – 630 nm, ET605/70, Chroma, USA). Each section was imaged by 7 % overlapping 1025x1025-µm tiles. A 16x water immersion objective lens (LWD 16x/0.80W; MRP07220, Nikon, Japan), with a resolution of 1 µm in X and Y and measured axial point spread function of ~5 µm full width at half maximum. After image acquisition, the raw images were stitched using a MATLAB-based software (StitchIt, https://github.com/BaselLaserMouse/StitchIt). The stitched images were then down-sampled by a factor of 25 in X and Y obtaining a voxel size of 25 x 25 x 25 µm, using a MATLAB-based software (MaSIV, https://github.com/alexanderbrown/masiv) to match the Allen Mouse Common Coordinate Framework version 3 (Wang et al., 2020). We used a MATLAB-based software (*ARA tools*, https://github.com/SainsburyWellcomeCentre/ara_tools) (Han et al., 2018) to register brain volumes and probe locations to the Allen mouse brain atlas. For some brains with DiI tracks, 100 µm thick serial sections were cut on a conventional vibratome. The slices were then mounted and imaged under a fluorescence microscope (Leica DM5500). MATLAB-based software (*Allen CCF tools*, https://github.com/cortex-lab/allenCCF) was used to register brain slices and probe locations to Allen mouse brain atlas (Shamash et al., 2018).

QUANTIFICATION AND STATISTICAL ANALYSIS

Wide-field imaging data

Sessions in which the difference between the Hit rate and False-alarm rate was larger than 0.1 or smaller than 0.2 were excluded from Novice and Expert sessions, respectively. In total, 62 Novice sessions and 82 Expert sessions from 7 RCaMP mice, and 57 Expert sessions from 7 tdTomato mice were used for analysis. Acquired images were down-sampled to 77x96 pixels (111 µm/pixel). For each trial, we calculated the normalized signal intensity of each pixel as $\Delta F/F_0 = (F-F_0)/F_0$, where F is the intensity of a pixel in each frame, and F_0 is the mean intensity of that pixel during the 1 second baseline period immediately before the onset of the visual cue. In each imaging session, mean $\Delta F/F_0$ images for different trial outcomes (Hit, Miss, False-alarm and Correct-rejection trials) were calculated by averaging “All” trials in each trial type, or by averaging “Quiet” trials in which mean jaw speed during 1 second delay period after the whisker stimulus did not exceed 4 times of the mean absolute deviation of the jaw speed (angle) during the 1 second baseline period in each trial. Images from different mice were horizontally shifted according to the functionally-identified C2-barrel (RCaMP mice) (Mayrhofer et al., 2019) and the cerebellar tentorium (RCaMP and tdTomato mice), and smoothed by spatial gaussian filter (sigma = 1 pixel, 111 μm). Those trial-averaged images in each session were used as individual samples for statistical analysis. To test statistical differences in the pixel values between different conditions, Wilcoxon’s rank-sum test was performed in each pixel, and *p*-value was corrected for multiple comparison by false-discovery rate, FDR (Benjamini and Hochberg, 1995). The corrected *p*-values were log-scaled ($-\log_{10}P$) to create spatial *p*-value maps. Borders between anatomical areas were drawn on the functional images (Vanni et al., 2017) by using Allen Mouse Common Coordinate Framework version 3 (CCF) (Lein et al., 2007; Wang et al., 2020) and ARA tools (Han et al., 2018; MacDowell and Buschman, 2020; Musall et al., 2019; Pinto et al., 2019). First, we defined the three dimensional location of bregma in 25-μm resolution Allen CCF by considering brain structures in the stereotaxic atlas (Paxinos and Franklin, 2019), and the thickness of skull (325 μm) (Soleimanzad Haleh et al., 2017). Second, the atlas was rotated by 24 degrees along the rostro-caudal axis. Third, anatomical borders were projected onto the horizontal plane to make a 24-deg tilted border map. Then, the border map was linearly scaled and horizontally shifted to match the functional images of RCaMP mice according to the C2-barrel, bregma, and the anteromedial end of the left hemisphere.

Electrophysiology data

Spiking activity on each probe was detected and sorted into different clusters using Klusta, an open source spike sorting software suited for dense multielectrode recordings (Rossant et al., 2016). After an automated clustering step, clusters were manually inspected and refined. Single units were categorized as regular spiking

(RSU) or fast-spiking neurons based on the duration of the spike waveform, and, in this study, we specifically focus on the putative excitatory RSUs (spike peak- to-baseline > 0.34 ms, 4415 units in Expert and 1604 units in Novice mice). Activity maps in Figure 3C and S6B were computed by averaging the trial-aligned peristimulus time histograms of all excitatory units recorded on the same probe.

Assessing Expert/Novice and Hit/Miss differences

Statistical difference between mean firing rates of Expert vs Novice (Figures 3C and 6D) and Hit vs Miss (Figure S3 and 6E) in each area was identified using non-parametric permutation tests in 50-ms bins and *p*-values were corrected by FDR.

Receiver Operating Characteristic (ROC) analysis

To quantify the selectivity of single units for Go vs No-Go trials we built ROC curves comparing distribution of spiking activity in bins of 100-ms including only correct trials (Hit and Correct-rejection). The area under the ROC curve was then compared to a baseline distribution (5 bins of 100-ms before visual cue onset) to examine the significance of selectivity beyond baseline fluctuations. Non-parametric permutation tests were performed and *p*-values were corrected by FDR and percentage of significant neurons in each area were identified (p<0.05, FDR-corrected, Figure 3E).

Clustering neuronal responses

For clustering the neuronal response patterns, RSUs from both Novice and Expert mice (1) with more than 200 spikes throughout the recording, and (2) with more than 5 trials for each trial-type (i.e. Hit, Miss, CR and FA) were included in the analysis (n=5405 out of 6019 RSUs). For each neuron and each trial type, time varying PSTHs (100 ms bin size) were computed over a 4 second window starting from 1 second before the visual cue and lasting until 1 second after the auditory cue. PSTHs from different trial types were baseline subtracted, normalized to the range of values across all bins and then concatenated resulting in an activity matrix $X \in \mathbb{R}^{5405 \times 160}$ whose row i corresponds to the concatenated normalized firing rate of the neuron i across different trial types (Figure S4A). Other normalization methods such as z-scoring resulted in similar clustering outcomes. To reduce the existing redundancy between firing rate time bins, we used Principle Component Analysis (PCA), and linearly projected firing rate vectors on a low-dimensional space. We applied PCA on the centered version of X (i.e. $x_i - \overline{x_\iota}.$) and found 14 significant components (permutation test with Bonferroni correction for controlling family wise error rate by 0.05) (Macosko et al., 2015). The weight of different components was equalized by normalizing the data resulting in unity variance for different components ($X' \in \mathbb{R}^{5405 \times 14}$).

Next, we employed spectral embedding on the data to detect non-convex and more complex clusters (Abbe, 2017; Von Luxburg, 2007). To do so, we computed the similarity matrix $S \in \mathbb{R}^{5405 \times 5405}$ whose element at row i and column j measures the similarity between ${x_i}'$ and ${x_j}'$ as

$$s_{ij} = \exp\frac{-||x_i' - x_j'\,||_2^2}{2\sigma^2} \in [0,1],$$

where σ is a free parameter determining how local similarity is measured in the feature space. We tuned σ by putting the average of similarity values equal to 0.5 (the tuned value for σ is 0.0987). Then, we computed the normalized Laplacian matrix as

$$L = I - D^{-0.5}\,WD^{-0.5}\,,$$

where I is the identity matrix, and D is the diagonal degree matrix defined as $\mathrm{diag}\left(\ \{\sum_{k=1}^{5405} s_{ik}\}_{i=1}^{5405}\ \right)$. The transformed features are rather abstract and computed as the eigenvectors of L. It should be noted that the new feature space is non-linearly transformed version of the PCA-space which is itself a linearly transformed version of the original firing rate space. Such a transformation is believed to naturally separate data points which are clustered together (Abbe, 2017; Von Luxburg, 2007). Using the elbow method on the eigenvalues of matrix L (i.e. finding the sharp transition in the derivative of sorted eigenvalues), we considered (after excluding the very 1st eigenvector) the first 13 eigenvectors of matrix L as representative features which yielded matrix $\tilde{X} \in \mathbb{R}^{5405 \times 13}$.

Finally, neurons were clustered based on the resulting matrix $\tilde{X}$ using a Gaussian Mixture Model (GMM). The algorithm considers that underlying distribution of data is a mixture of K Gaussians with means $\{\mu_1, \ldots, \mu_k\}$, diagonal covariance matrices $\{\Sigma_1, \ldots, \Sigma_k\}$, and weights $\{p_1, \ldots, p_k\}$. For a given K, we estimated the parameters of this mixture model by using expected maximization (EM) algorithm (5000 repetitions and 1000 iterations). The number of clusters was then selected ($K = 24$) by minimizing the Bayesian information criterion (BIC) (Engelhard et al., 2019) (Figure S4B). Using the fitted parameters, we assigned a cluster index $c_i \in \{1, \dots ,24\}$ to each neuron corresponding to the Gaussian distribution it belongs (with the highest probability). The output of GMM step was the vector $C \in \{1, \dots ,24\}^{5405}$ containing the cluster indices of neurons.

To study the patterns captured by different clusters, we first quantified the proportion of neurons within each cluster belonging to either Expert or Novice mice. To account for the differences in the total number of neurons belonging to each group (n=3960 neurons from Expert, n=1445 neurons from Novice), weighted proportions were considered. Next, for each cluster, we quantified the distribution of neurons across different brain regions in Novice and Expert mice (Figure 4B-C, S4C). Similarly, in computing these distributions, weighted proportions were considered to correct for the difference in sample sizes. In addition, for selected clusters (Figure 4C, right panel), 2D-maps were computed by plotting the spatial distribution of neurons (based on their reconstructed anatomical location) across dorsal cortex in bins of 50x50 μm – the value for each bin was normalized by total number of neurons within the bin. These maps were then smoothed using a 2-D Gaussian kernel (sigma=150 μm).

To characterize changes across learning of the delay task in each area, we computed separately in Novice and Expert mice, the activity pattern of the two most representative clusters (i.e. clusters with the highest number of neurons among all clusters) (Figure 4D and S4D) by averaging the activity among neurons belonging to the pair of area and cluster.

GLM encoding model

We used Poisson regression to fit an encoding model (Generalized linear model, GLM) to predict the spiking activity of each individual neuron given behavioral data (Nelder and Wedderburn, 1972; Park et al., 2014). For each session, we concatenated all correct trials (Hit and Correct-rejection) and then split the data to perform five-fold cross-validation. In Poisson regression, one aims at predicting the spike count Y(t) in a time bin t according to the formula:

$$Y(t) \sim \mathrm{Poisson}\left(e^{X \cdot \beta}\right),$$

i.e. assuming that the spike counts are sampled from a Poisson distribution with rate that depends on the design matrix X and on the weight vector β. In our case, Y was constructed by binning the spikes in 100 ms bins. The weights β were fit by maximizing the likelihood with Ridge regularization for each fold, and then averaged across the five folds. The parameter that controls the strength of the regularization was determined separately for each neuron using evidence optimization (Cunningham et al., 2008; Park et al., 2014).

The design matrix was constructed by including three types of variables: “event” variables, associated to task-related events; “analog” variables, associated to real-valued behavioral measures from videography; and “slow” variables, which were constant during one trial but could vary over the course of one session. Event variables included the visual cue onset, the whisker stimulus onset, the auditory cue onset and the onset of the first lick. The exact time of lick onset was determined from the high-speed video using a custom algorithm. To assess the delayed effect of such task-related variables, each of these event-like variables was associated with a set of ten 100-ms wide and unit height boxcar basis functions, spanning in total one second after each event. The first-lick variable was associated with two additional boxcar functions covering 0.2 seconds prior to the lick onset, to capture lick-specific preparatory neuronal activity. Analog variables included in the design matrix were the whisker, tongue and jaw speed. These quantities were first extracted from the high-speed videos using custom code and then averaged in 100 ms bins. Among the slow variables, we included the trial index, i.e. a variable that at each trial k took a constant value equal to $k/_{k_{total}}$, where k_{total} is the total number of trials in a session. This variable could capture shifts in a neuron baseline activity due to slow effects across the session such as changes in satiety and motivation. Finally, we included three binary variables that took value one only if the previous trial was an early lick, a False-alarm or a Hit trial, to capture the effect of the previous trial outcome on the subsequent trial. In total, our design matrix had 50 columns, corresponding to the number of free parameters of the model.

To assess the significance of each variable in the design matrix, we fitted a new GLM model obtained by removing the variable of interest (reduced model) from the full model. If for a certain neuron the reduced model fitted the data significantly worse than the full model (*p*<0.05, according to a likelihood ratio test (Buse, 1982), then that neuron was considered significantly modulated by the removed variable. The reduced model was fitted independently for each fold, using the same data splitting used for the full model. In the likelihood ratio test, the test statistics are given by $2\log({}^{L_{full}}/_{L_{reduced}})$, where L_{full} and $L_{reduced}$ are the full and reduced model likelihood respectively. These statistics were computed for each fold and then averaged to obtain an average statistic, from which the final *p*-value was computed (Buse, 1982). Note that in the presence of correlations among variables, this approach is stringent in that it tends to underestimate the significance of different variables. To separately assess the effect of the onset of event-like variables from their delayed effects, we quantified their significance independently by separately removing the first two basis functions or remaining eight basis functions (Visual, Auditory and Lick). For the whisker variable, since it was very brief in time (10 ms), we removed either the first or the remaining nine bins (referred to as ‘Whisker’ and ‘Delay’ respectively in Figure 5D and 5E). To assess the significance of the modulation due to lick-preparatory neuronal activity we separately removed the two basis functions that preceded the lick onset (referred to as ‘PreLick’ in Figure 5D and 5E). Spatial weight maps for selected model variables (Figure 5C, right panel) were built by first averaging the weights over the time course of the variable, i.e. by averaging over the weights of the boxcar basis functions. Next, for each neuron these weights were projected on the reconstructed anatomical location in 2D, and were then averaged across all neurons with a certain spatial bin (50x50 µm). The resulting spatial weight map was smoothed using a 2D Gaussian kernel (sigma=150 µm). All the GLM analysis was performed in MATLAB using a combination of existing and custom-written code.

Assessing optogenetic inactivation impact

To quantify the impact of optogenetic inactivation we compared mouse averaged performance (n=9; Hit rate, False alarm rate and Early lick rate) for different light windows (i.e. Baseline, Whisker, Delay, Response) to light-off control trials. P-values were corrected for multiple comparison (i.e. 4 windows) using Bonferroni correction.

Quantifying involvement index

The involvement index was defined by combining the neuronal correlates and behavioral impact of optogenetic inhibition. For each pair of area and temporal window of interest, we built two distributions of bootstrap estimation of the mean, separately for neuronal correlates and inhibition impact, by bootstrapping 1000 times. The neuronal correlates were quantified as the mean firing rate difference in Hit vs Correct rejection trials across all neurons recorded from 25 Expert mice. The inhibition impact was quantified as the mean change in Hit rate across 9 VGAT-ChR2 mice. The distribution of involvement index was calculated as the product distribution of the two bootstrap distributions.

Statistics

Data are represented as mean ± SEM unless otherwise noted. The Wilcoxon signed rank test was used to assess significance in paired comparisons; and the Wilcoxon rank sum test was used for unpaired comparisons (Matlab implementations). Analysis of spiking activity and involvement index was performed using a non-parametric permutation test. The statistical tests used and n numbers are reported explicitly in the main text or figure legends.

Data and code availability

The complete data set and Matlab analysis code will be made freely available at the open access CERN Zenodo database https://zenodo.org/communities/petersen-lab-data.